TECHNISCHE
UNIVERSITÄT
WIEN
Vienna University of Technology

DIPLOMARBEIT

Assembling and Testing a Device for a Synthesis of Thin Film Heusler Systems

ausgeführt am Institut für Festkörperphysik
der Technischen Universität Wien

unter der Anleitung von
Univ.Prof. Dipl.-Ing. Dr.techn. Ernst Bauer

durch

Matthias Scattolin
00525385

Angeligasse 116/24,
1100 Wien

31. August 2020

Abstract

The goal of this thesis was the design and assembly of a magnetron sputter for the production of thin films on glass and silicon wafers and the analysis of the thermoelectric properties of these samples. To verify the quality of the produced films a profilometer was used to measure the film thickness, as well as the surface quality. Later samples were analysed in a $\theta - \theta$ x-ray diffractometer. This made it possible to verify the expected crystal structure of the material used. Best results were achieved when using a sputter power of 13 watts, leading to a sputter rate of about 0,07 µm per minute. The Seebeck coefficient of some samples was measured and showed that this magnetron sputter can be used for future experiments to continue the analysis of the thermoelectric properties of thin film Heusler compounds. The materials used were mainly based on the Heusler compound Fe_2VAl.

Kurzfassung

Das Ziel dieser Diplomarbeit war die Planung und der Aufbau einer Magnetronsputteranlage zur Herstellung dünner Schichten auf Glas und Siliziumwafern, sowie die anschließende Untersuchung thermoelektrischer Eigenschaften dieser Schichten. Die Qualität der produzierten Proben wurde zu Beginn über die Oberflächenstruktur und Schichtdicke mittels eines Profilometers verifiziert. Spätere Proben wurden zusätzlich mit Hilfe eines $\theta - \theta$ Röntgendiffraktometers untersucht. Dies diente zur Feststellung, ob die Schichten die gewünschte Kristallstruktur aufweisen. Die besten Ergebnisse wurden bei einer Sputterleistung von 13 Watt erzielt, was einer Beschichtungsrate von etwa 0,07 µm pro Minute entsprach. Weiters wurde von einigen Proben der Seebeck-Koeffizient gemessen. Die Ergebnisse zeigten, dass die Anlage für zukünftige Experimente verwendet werden kann, um die thermoelektischen Beschaffenheiten von Heuslermateriealien weiter zu erforschen. Die verwendeten Materialien basierten auf Heuslerverbindungen vom Typ Fe_2VAl.

Acknowledgements

First, I would like to thank my supervisor Ernst Bauer for the possibility to work on this topic. His positivity and encouragement always were a source of motivation and the main reason for the pleasant atmosphere in the entire group.

This leads me to thanking my colleagues, especially Bernhard Hinterleitner, who helped with a lot of design problems in the early stage of this thesis. Special mention to Michael Parzer and Alexander Riss for helping out with some measurements and being the first people to actually use the new sputter.

Thanks to all my friends from university and to all the lovely people from the Fachschaft Physik and the HTU who made all these years a wonderful time. Out of all these people the "Generation Rosa" is the best and will always be an important part of my life.

Also a thank you to Peter and Conny for providing the little push I needed from time to time to keep on going, and Beauty for the awesome photographs.

I want to mention the Stipendienstelle. Their Studienabschluss-Stipendium made it possible for me to quit my job and come back to university to work on my diploma thesis and finally finish my studies.

Also a big thank you to my family for their support and believing in me. I am happy to finally say to my mother: "Hiermit präsentiere ich dir endlich deinen persönlichen Diplom-Ingenieur!"

Thank you all!

Contents

1. Introduction

With the ever growing energy demand of humanity and its consequences on global warming and therefore changing climate, it is more important than ever to find ways to counter this trend. Increasing energy efficiency by utilizing waste heat is one way to archive this goal. High performance thermoelectrics are essential in converting previously unused heat into electrical energy. The central part of this thesis is the creation of thin films Heusler compounds with very promising thermoelectric properties. The ongoing research on these materials could lead to new viable methods to increase the energy efficiency of various existing machines and therefore reduce their overall energy demand.

The first three chapters discuss the theoretical background of thermoelectric properties in general, the nature of Heusler compounds and the principals of DC magnetron sputtering. Following, is the setup of the sputter installation, including its design and construction phases. Chapter 8 shows a detailed explanations of the measurements of the thin film samples produced. The diploma thesis is then closed with a conclusion and possible future enhancements for the sputter installation.

2. Transport Phenomena

The term *Transport Phenomena* is used to describe a number of processes in solid state structures. Typical, and for this thesis most relevant examples are electrical and thermal conductivity and the Seebeck effect. This chapter describes methods, which help to understand and account for these processes. To identify efficient thermoelectric materials, two parameters are introduced. The power factor PF and the figure of merit, with the latter usually called *ZT value*, are a combination of these before mentioned parameters and quantify the efficiency of a thermoelectric material (Chapter 2.5). The structure and explanations are inspired by references [6], [4] and [7]. Observations show that heat flows along a gradient in temperature, from warmer areas to colder ones. This can be written as

$$\vec{j} = -\lambda \vec{\nabla} T \,,$$

with $\vec{j}$ being the heat flux vector and $\vec{\nabla} T$ the temperature gradient. The thermal conductivity coefficient λ, which is dependent on the material, is proportional to the specific heat of the material, as well as the velocity and the mean free path of the contributing particles. To describe λ in solids, a model of the crystalline lattice is used. In this model there are two main contributors to the thermal conductivity: free electrons and lattice waves.

2.1. Thermal Conductivity

A perfect crystal has a periodic potential with periodic boundary conditions and can be written as

$$U(\vec{r}) = U(\vec{r} + \vec{T}) \,,$$

with $\vec{T}$ being the translation vector. Moving particles, in this case free electrons, can be described as Bloch-waves

$$\psi_{\vec{k}}(\vec{r}) = u_{\vec{k}}(\vec{r})e^{i\vec{k}\vec{r}}\,,$$

where $\vec{k}$ is the wave vector showing the same periodicity as the crystal lattice

$$u_{\vec{k}}(\vec{r}) = u_{\vec{k}}(\vec{r}+\vec{T})\,.$$

With the momentum $\vec{p} = \hbar\vec{k}$, the energy can be written as a function of $\vec{k}$. The periodic lattice can be transformed to its reciprocal lattice in $\vec{k}$ space. The reciprocal translation vector $\vec{G}$ can be defined as $\vec{G} = h\vec{g_1} + k\vec{g_2} + l\vec{g_3}$, with hkl being called Miller Indices. The reciprocal basis vectors $\vec{g_i}$ are given as

$$\vec{g_i} = \frac{2\pi}{V_E}\vec{b_j} \times \vec{b_k}\,.$$

The vectors $\vec{b_i}$ are the basis vectors in real space and V_E is the volume of the elementary cell. The wave function and the dispersion relation are both periodic in $\vec{k}$ space.

$$\psi_{\vec{k}}(\vec{r}) = \psi_{\vec{k}+\vec{G}}(\vec{r})$$
$$E(\vec{k}) = E(\vec{k}+\vec{G})$$

Thanks to the periodicity, only the first period is needed for a complete description and is called the first Brillouin zone. Considering the periodic lattice, $\vec{k}$ can only take discrete values. According to the Pauli exclusion principle, each of these states can contain a maximum of two electrons (one spin up and one spin down). Resulting from defects in the periodicity of the lattice, in reality the wave functions are only quasi-stationary states. Since it is not feasible to calculate every single one of these quasi stationary states, the statistically average occupation number in a thermodynamic equilibrium is used. The occupation number f_0 of a given state $\vec{k}$ is given by

$$f_0(\vec{k}) = \left(e^{\dfrac{E(\vec{k})-\mu}{k_BT}} + 1\right)^{-1}$$

and is called Fermi-Dirac distribution, with μ being the chemical potential and k_B being the Boltzmann constant.

The deduction of transport phenomena is done by calculating the distribution in dependence of external fields, $f(\vec{r}, \vec{k}, t)$. Under the influence of an external field the distribution is no longer in a homogenous equilibrium, but is dependent on space and time. In the time interval $[t \rightarrow t + dt]$ the distribution function changes from

$$f(\vec{r}, \vec{k}, t) \rightarrow f(\vec{r} + \dot{\vec{r}}dt, \vec{k} + \dot{\vec{k}}dt, t + dt) = f(\vec{r}, \vec{k}, t) + \left(\frac{\partial f}{\partial t}\right)_{collision} dt$$

to the Boltzmann equation

$$\left(\frac{\partial}{\partial t} + \dot{\vec{k}}\vec{\nabla}_{\vec{k}} + \dot{\vec{r}}\vec{\nabla}_{\vec{r}}\right) f\left(\vec{r}, \vec{k}, t\right) = \left(\frac{\partial f}{\partial t}\right)_{collision} .$$

An external electrical field interacts with the electrons and causes a change in their momentum $\hbar\dot{\vec{k}} = e\vec{E}$ with the electric field $\vec{E}$ and the electric charge of the electron e. A temperature gradient causes a spacial dependency of the electron distribution. Therefore, the Boltzmann equation can be written as

$$\frac{df}{dt} = -\vec{v}\vec{\nabla}_{\vec{r}}f + \frac{e\vec{E}}{\hbar}\vec{\nabla}_{\vec{k}}f + \left(\frac{\partial f}{\partial t}\right)_{collision} .$$

To calculate this formula analytically, two assumptions are made. Firstly, the difference between the non-equilibrium distribution and the equilibrium distribution $g(\vec{k}) = f(\vec{k}) - f_0(\vec{k})$ is proportional to the external forces and it is small. Secondly, scattering processes caused by lattice vibrations and defects in the crystal structure are countering the external disturbances. With the assumptions in place, these external disturbances of the equilibrium distribution can be described by the relaxation time ansatz

$$\left(\frac{df}{dt}\right)_{collision} = -\frac{g(\vec{k})}{\tau(\vec{k})} ,$$

with the relaxation time τ.

The relaxation process will lead to a stationary state under the influence of a constant external force. This means that the first term of the Boltzmann equation $\dfrac{\partial f}{\partial t}$ equals zero. Now $g(\vec{k})$ can be written as

$$g(\vec{k}) = -\tau(\vec{k})\frac{df_0}{dE}\vec{v}\left(e\vec{E} - k_B\left(\frac{E-\mu}{k_BT} + \frac{1}{k_B}\frac{d\mu}{dT}\right)\vec{\nabla}T\right) .$$

With $g(\vec{k})$ known, the electrical current density can be expressed as

$$\vec{j}_e = \frac{e}{4\pi^3}\int \vec{v}(\vec{k})g(\vec{k})d^3\vec{k} \, ,$$

analogous the thermal current density can be written as

$$\vec{j}_Q = \frac{1}{4\pi^3}\int \vec{v}\left(E(\vec{k}) - \mu\right)g(\vec{k})d^3\vec{k} \, .$$

Instead of integrating a volume in $\vec{k}$ space, $\vec{j}_e$ and $\vec{j}_Q$ are converted to an integration of a surface of constant energy dS_E,

$$d^3\vec{k} = dS_E d\vec{k}_\perp = dS_E\frac{dE}{\vec{\nabla}_{\vec{k}}E} \, .$$

With $\vec{j}_e = \sigma_{ij}\vec{E}$ and $g(\vec{k})$ being a function of $\frac{df_0}{dE}$, the conductivity tensor can be written as

$$\sigma_{ij} = \frac{e^2}{4\pi^3}\int v_i(\vec{k})v_j(\vec{k})\tau(\vec{k})\frac{dS_E dE}{\vec{\nabla}_{\vec{k}}E} \, .$$

In the case of no electrical current ($\vec{j}_e = 0$), the current densities can be written in dependence on $\sigma(E)$, which leads to an equation of the form $\vec{j}_Q = -\lambda_{electron}\vec{\nabla}T$:

$$\lambda_{electron} = \frac{k_BT}{e^2}\left(K_2 - \frac{{K_1}^2}{K_0}\right) .$$

with

$$K_m = -\int \sigma(\epsilon)\epsilon^m\frac{df_0}{d\epsilon}d\epsilon \quad \text{and} \quad \epsilon = \frac{E-\mu}{k_BT} \, .$$

The second major contribution to the thermal conductivity comes from the vibrations of the lattice. The atoms in a lattice structure are not fixed on their places, but vibrate around their equilibrium position. These oscillations can be described as harmonic oscillators. The equilibrium position is not fixed but dependent on the position of the neighbouring atoms. Therefore, the harmonic oscillators are coupled to each other. The coupled system can be seen as a superposition of propagating lattice waves. The displacement from the equilibrium position is

$$\vec{u}(\vec{r}) = \sum_{\vec{q}} u_0 e^{i(\vec{q}\cdot\vec{r}+\omega t)}$$

with $\vec{q}$ as wave vector.

Analogous to the electronic contribution above, the same restrictions induced by the periodicity of the lattice are applied. The wave vector $\vec{q}$ is quantised and only the first Brillouin zone is needed for a description of physical properties. The waves can be differentiated by the polarisation of the oscillation. There are two transversal waves with a polarisation perpendicular to $\vec{q}$ and one longitudinal wave with a polarisation parallel to $\vec{q}$. All three of these vectors are mutually perpendicular to each other.

In a lattice with two or more atoms in its irreducible unit cell are $3r$ different modes, with r being the number of different atoms. The first 3 modes are the *acoustic* modes, the remaining $3r - 3$ modes are *optical* modes.

Each of these modes can possess a discrete energy given by their description as a harmonic oscillator,

$$E(\vec{q}) = \hbar\omega \left(n + \frac{1}{2}\right) ,$$

with the integer $n \geq 0$. These discrete steps in energy are called phonons and are described as quasi-particles moving through the lattice. Phonons are bosons and therefore the equilibrium distribution can be described with the Planck-distribution, which is a special case of the Bose-Einstein statistics

$$N_0(\vec{q}) = \left(e^{\frac{\hbar\omega}{k_B T}} - 1\right)^{-1} .$$

In the case of a temperature gradient $\vec{\nabla}T$, an ansatz similar to electronic contribution can be used,

$$\frac{dN}{dt} = -\vec{v}_g \vec{\nabla} N_0 \,,$$

where $\vec{v}_g = \dfrac{\partial \omega}{\partial \vec{q}}$ is the group velocity. The tendency of scattering processes countering the disturbances of the equilibrium can be described again with the relaxation time ansatz

$$\frac{dN}{dt} = -\frac{N(\vec{q}) - N_0(\vec{q})}{\tau(\vec{q})} = -\frac{n(\vec{q})}{\tau(\vec{q})} \,,$$

with $n(\vec{q})$ being the deviation from the equilibrium. Eventually, a steady state will be reached when $\dfrac{dN}{dT} = 0$ and it can be written as

$$n(\vec{q}) = -\tau(\vec{q})\vec{v}_g \cdot \vec{\nabla} T \frac{dN_0}{dT} \,.$$

The heat current density $\vec{j}(Q)$ can then be written as a function of the deviation,

$$\vec{j}_Q = \sum_{\vec{q}} \vec{v}_g \hbar \omega n(\vec{q}) \,.$$

As before, $\vec{j}_Q = -\lambda_{lattice} \vec{\nabla} T$ can be used for the lattice contribution to the thermal conductivity to obtain

$$\lambda_{lattice} = \sum_{\vec{q}} (\vec{v}_g \cdot \vec{e}_Q)^2 \tau(\vec{q}) c(\vec{q}) \,,$$

where $\vec{e}_Q$ is the direction of the heat flow and $c(\vec{q})$ is the specific heat of a mode $\vec{q}$. Finally, the total thermal conductivity can be written as

$$\lambda = \lambda_{electron} + \lambda_{lattice} \,.$$

2.2. Scattering Processes

Interactions between electrons $\vec{k}$ and/or phonons $\vec{q}$ are needed to change from one energy state to another ($E_j = E_i + \Delta E$). The interaction can be written as a vector addition of the involved wave vectors. In the case of phonons ($\vec{q} + \vec{q}' \rightarrow \vec{q}''$)

it is written as

$$\vec{q} + \vec{q}' - \vec{q}'' = 0\,.$$

Processes following this equation are described as *normal processes* and are therefore called *N-processes*. With consideration of the periodicity of the potential and that every point is equal to a point in the first Brillouin zone by shifting it by the reciprocal lattice vector $\vec{G}$, we obtain

$$\vec{q} + \vec{q}' - \vec{q}'' = \vec{G}\,.$$

If the sum of $\vec{q}$ and $\vec{q}'$ is outside the first Brillouin zone, it can be returned by subtracting $\vec{G}$. This means, $\vec{q}''$ can change direction and the corresponding momentum $\hbar\vec{G}$ is transferred to the lattice. These processes are called *umklapp processes*, or *U-processes*.

N-processes do not change the momentum of the phonons and therefore have no contribution to thermal conductivity. The change of a phonon's momentum by $\hbar\vec{G}$ during a U-process is the dominant contributor to the thermal resistivity.

2.3. Electrical Conductivity

A solid conductor can be seen as a lattice of relatively immobile positive ions. Electrons are moving in the lattice and are constantly bouncing against the much heavier ions. This model by Paul Drude is based on the kinetic theory of gases with the following assumptions: Electrons do not interact with other electrons and electron ion collisions are elastic. With the introduction of an electric field $\vec{E}$ the electrons e experience an acceleration in a specific direction. The equation of motion for the electrons can be written as

$$m\frac{d\vec{v}_{drift}}{dt} + \frac{m}{\tau}\vec{v}_{drift} = -e\vec{E}\,,$$

with m being the mass of an electron, e its elemental charge and τ the mean free time between two collisions. The drift velocity is the average of the electron velocity minus the Fermi velocity $\vec{v}_{drift} = \langle\vec{v} - \vec{v}_{Fermi}\rangle$. The Drude model also states, that the gained velocity is lost with the next collision. For the stationary state ($\frac{d\vec{v}}{dt} = 0$) the drift velocity can be expressed as

$$\vec{v}_{drift} = -\frac{e\tau\vec{E}}{m} \,.$$

With the charge carrier density n and the movement of the electrons $e\vec{v}_{drift}$, the electrical current can be written as

$$\vec{j} = -en\vec{v}_{drift} = \frac{e^2 n\tau}{m}\vec{E} = \sigma\vec{E} \,,$$

which is better known as *Ohm's law*, with σ being the electrical conductivity. The electrical resistivity ρ is given by

$$\rho = \frac{1}{\sigma} = \frac{m}{e^2 n\tau} \,.$$

To describe the temperature dependence of the electrical resistivity of metals, ρ can be written according to the Matthiessen rule as

$$\rho = \rho_{defect} + \rho_{phonon} + \rho_{electron} + \ldots \,,$$

where ρ_{defect}, ρ_{phonon} and $\rho_{electron}$ are the contributions to the resistivity by the electrons scattered at crystal defects, phonons, or other electrons. The largest contribution for metals around room temperature is ρ_{phonon} and given by the Bloch-Grüneisen formula

$$\rho_{phonon}(T) = A\left(\frac{T}{\Theta_D}\right)^5 \int_0^{\frac{\Theta_D}{T}} \frac{x^5 dx}{(e^x - 1)(1 - e^{-x})} dx \,,$$

with A being a constant factor and Θ_D the Debye temperature. For high temperatures ($T \gg \Theta_D \rightarrow x \ll 1$) the integral is proportional to $(\frac{\Theta_D}{T})^4$ and therefore

$$\rho_{phonon}(T \gg \Theta_D) \propto \frac{T}{\Theta_D} \,.$$

In the case of low temperatures ($T \ll \Theta_D$) the integral becomes constant and the resistivity

$$\rho_{phonon}(T \ll \Theta_D) \propto (\frac{T}{\Theta_D})^5 \,.$$

This shows that over the entire temperature range, the resistivity of metals increases with the temperature.

In contrast to metals, semiconductors do not have a constant number of electrons in the conduction band. With σ being proportional to the charge carrier density

$$n(T) = \int_{\epsilon_f}^{\infty} N(\epsilon) f(\epsilon, T) d\epsilon \,,$$

with the Fermi energy ϵ_f, the density of state $N(\epsilon)$ and the Fermi distribution $f(\epsilon, T)$. The charge carrier density grows exponentially, which, in general, is stronger than the phononic contribution to the resistivity. Therefore, the resistivity of semiconductors falls with rising temperature. Materials with properties of metals and semiconductors can for example behave like metals at high and low temperatures, but only at a specific temperature range the resistivity drops with rising temperature.

2.4. Seebeck Coefficient

With the consideration of a non zero temperature gradient ($\nabla_{\vec{r}} T \neq 0$) and an external field $\vec{E}$, the relaxation time ansatz of the non-equilibrium distribution can be written as

$$f(\vec{k}) = f_0(\vec{k}) + \frac{e\tau}{\hbar} \vec{E} \nabla_{\vec{k}} f - \tau \vec{v} \nabla_{\vec{r}} f \,.$$

With only small disturbances the equation can be linearised to

$$f(\vec{k}) \simeq f_0(\vec{k}) + \frac{e\tau}{\hbar} \vec{E} \nabla_{\vec{k}} f_0 - \tau \vec{v} \frac{\partial f_0}{\partial T} \nabla_{\vec{r}} T \,,$$

which again leads to an equation of the current density (in direction $\hat{e}_x$)

$$j_x = \sigma E_x - \int \tau v_x^2 \frac{\partial f_0}{\partial T} \frac{\partial T}{\partial x} d^3k \, .$$

The transport coefficients $\mathcal{L}^{ij}$ allow for a clearer notation for j_e and j_Q,

$$j_e = \mathcal{L}^{11} \vec{E}' + \mathcal{L}^{12}(-\nabla T) \, ,$$

$$j_Q = \mathcal{L}^{21} \vec{E}' + \mathcal{L}^{22}(-\nabla T) \, .$$

$\vec{E}' = \vec{E} + \frac{1}{e} \nabla_{\vec{r}} \mu(\vec{r})$ considers the gradient of the chemical potential. For $j_e = 0$ follows

$$\vec{E} = (\mathcal{L}^{11})^{-1} \mathcal{L}^{12} \nabla T = S \cdot \nabla T \, ,$$

where $S = (\mathcal{L}^{11})^{-1} \mathcal{L}^{12}$ is the Seebeck coefficient.

2.5. ZT Value and Power Factor

As mentioned in the beginning of this chapter, the electrical and thermal conductivity, as well as the Seebeck coefficient, all contribute to the efficiency of a given material. Therefore, it is useful to combine these parameters to quantify thermoelectric properties. The ZT value, or figure of merit, describes the efficiency of a thermoelectric material,

$$ZT = \frac{S^2 \sigma}{\kappa} T = \frac{PF}{\kappa} T \, ,$$

with the power factor $PF = S^2\sigma$, Seebeck coefficient S, electrical conductivity σ, thermal conductivity κ and the temperature T. This means good thermoelectric materials have a high Seebeck coefficient, high electrical conductivity and low thermal conductivity. A higher power factor means the potential to 'generate' more electric energy. Therefore, the Seebeck coefficient, the electrical resistivity and the thermal conductivity are the most important parameters for the identification of high performance thermoelectric materials.

3. Heusler Compounds

Heusler compounds are named after Fritz Heusler, who discovered an interesting magnetic behaviour of Cu_2MnAl, which consists of only non-magnetic materials in 1903. Today, this category contains over 1000 compounds, many being still actively researched. In general, these compounds are divided into two categories. *Half-Heusler*, with a stoichiometry of 1 : 1 : 1 and *full-Heusler* or simply *Heusler*, which have a 2 : 1 : 1 stoichiometry. For the presented work, only full-Heusler are relevant and discussed in more detail with a special focus on Fe_2VAl. A comprehensive overview is given by T. Graf et al. [8].

3.1. Crystal Structure

In general, Heusler compounds are the composition X_2YZ of the three elements X, Y and Z. This compound forms a cubic space group $Fm\bar{3}m$ (space group no.225) crystal structure. The X atoms are on the Wyckoff position 8c, which corresponds to plane $(\frac{1}{4},\frac{1}{4},\frac{1}{4})$, the Y atoms are at position 4a / plane (0,0,0) and Z atoms on 4b / $(\frac{1}{2},\frac{1}{2},\frac{1}{2})$. This structure can be seen as an interconnection of four face centered cubic lattices (*fcc*), two are occupied with X, one with Y and one with Z. The X lattices are then alternately interwoven with the Y and Z equivalents.

Another way to describe the Heusler crystal is as a CsCl like structure, which is the Heusler structure shifted by $(\frac{1}{4},\frac{1}{4},\frac{1}{4})$, with X atoms on the Cs positions and Y,Z alternately on the Cl positions. These visualisations can be seen in figure 3.1, which shows the $Fm\bar{3}m$ space group in the case of Fe_2VAl modelled with the software PowderCell and figure 3.2, which shows the CsCl like substructures within the Heusler lattice. With Fe_2VAl being only one of many possible Heusler compounds, the colour coded periodic table in figure 3.3 shows the sheer number of possible

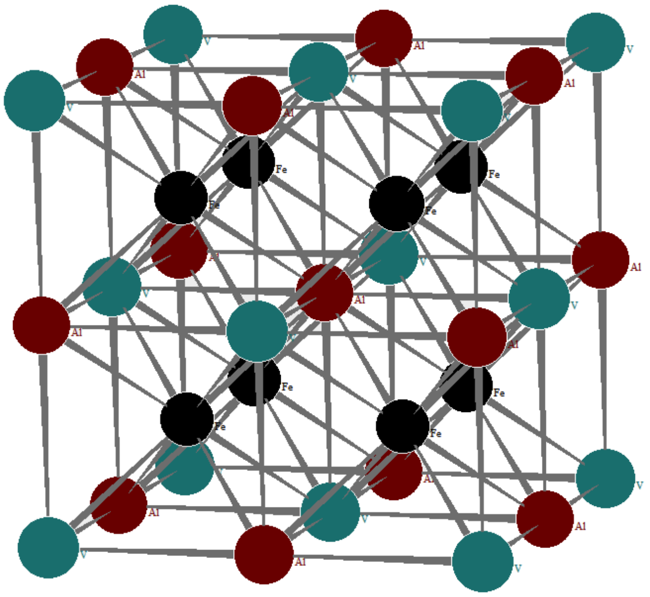

Figure 3.1.: The Heusler structure of Fe_2VAl modelled with the software PowderCell. Positions of the iron atoms are marked black, vanadium positions are blue and the aluminium positions are red.

combinations of elements to form Heusler compounds. The colours correspond to the possible X, Y and Z positions in the lattice. This hints the possibility to dope the compound with other compatible materials. An example is $Fe_2V_{0.8}W_{0.2}Al$, with a 20 percent substitution of vanadium (V) atoms with tungsten (W) atoms.

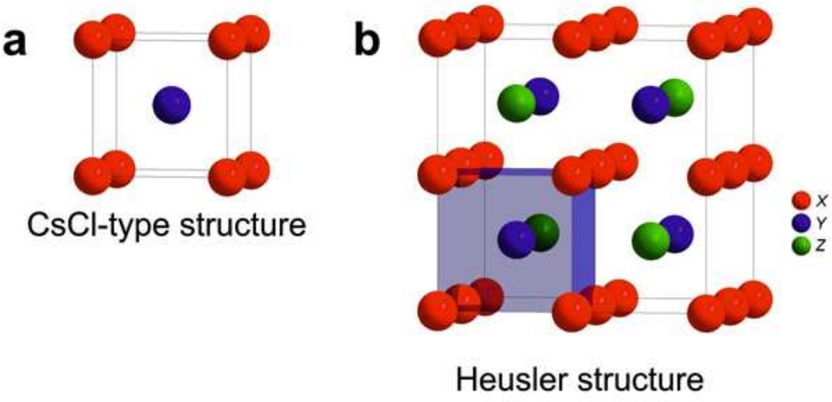

Figure 3.2.: CsCl structure (a) in comparison to the by $(\frac{1}{4},\frac{1}{4},\frac{1}{4})$ shifted Heusler structure (b), which can be seen as CsCl like substructures next to each other with element X on the Cs position and alternating elements Y and Z on the Cl positions. Courtesy of [8].

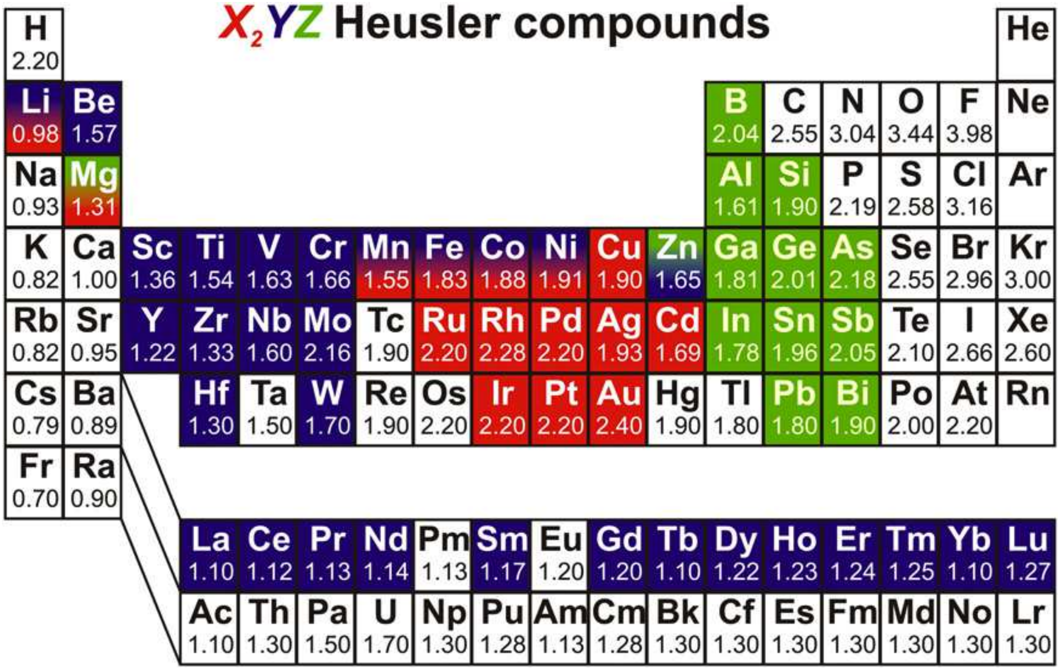

Figure 3.3.: Colour coded periodic table that shows the numerous possible combinations of elements to form Heusler compounds of a X_2YZ structure. The colours represent the possible positions an element can take within the crystal. Courtesy of [8].

3.2. Band Structure

A convenient feature of Heusler compounds is that many properties can be predicted by the number of valence electrons in the material. In the case of Fe_2VAl (Fe_2: $8+8$, V: 5, Al: 3) this number is a total of 24 valence electrons, which predicts a semiconductor. A closer look at the energy states shows a zinc-blende-like sublattice [FeAl]. The s and p orbitals split into a set of bonding and a set of anti-bonding states. The *3d* states of the iron split between d_{z^2}, $d_{x^2-y^2}$ (e) and d_{xy}, d_{xz}, d_{yz} (t_2) (figure 3.4 (a)).

The combination of this [FeAl] structure, the second Fe and the V atom can be seen in figure 3.4 (b). The t_2 and e states from the [FeAl] substructure and the *3d* states from the second Fe atom split again. The orbitals of the vanadium atom are in between the split orbitals and form a small band gap around the Fermi level. The very narrow band gap around the Fermi energy means that even a small disorder can lead to a loss of the semiconducting characteristics and the appearance of magnetism.

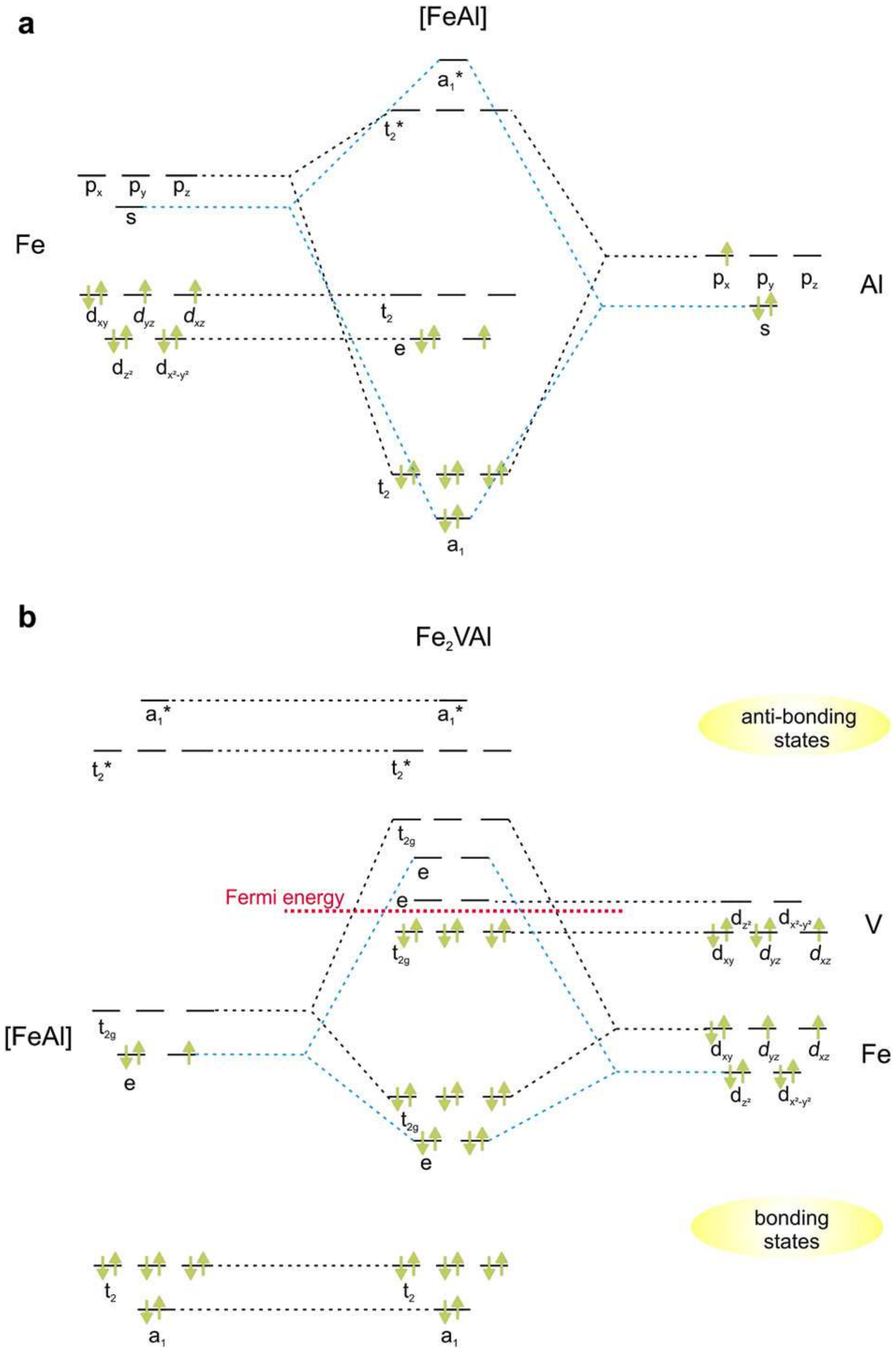

Figure 3.4.: Illustration of the orbital structure of Fe_2VAl. (a) Hybrid orbitals of the [FeAl] substructure. (b) Interaction of the substructure with the second Fe and the V atom and the position of the Fermi energy in a narrow band gap between the vanadium orbitals. Courtesy of [8].

4. DC Magnetron Sputter

Sputter are devices that are used to coat surfaces with very thin films of solid materials. They are used in science experiments as well as large industrial production lines. DC magnetron sputtering being one possible technology to realise a Sputter. The main advantages of DC magnetron sputtering over conventional DC sputtering are higher sputter rates and lower argon pressure as discussed in [2]. Compared to conventional DC sputtering, permanent magnets are positioned behind the sputter target in a way that the magnetic field lines are formed in front of the mounted target material. Free electrons in the vicinity of the sputter head are trapped on a helix around this magnetic field lines instead of being able to escape. This leads to a higher electron concentration near the target surface. Figure 4.1 shows the principle of the sputter head, as well as the practical realisation with cylindrical permanent magnets to form the magnetic field in front of the target material. The outer magnets are all parallel polarised, in contrast the single magnet in the middle is polarised in the opposite direction.

The chamber is filled with a low pressure argon atmosphere. Argon atoms have a chance to get ionised by the trapped electrons. These ions are attracted by the negative charge of the target. Ions with enough energy are able to knock out atoms from the target material which travel into the chamber. As a result, when a substrate is placed in front of the sputter head it is coated with a thin film of the target material. The pressure has to be finely adjusted. It needs to be sufficiently high to produce enough ions to actually get the sputtering started and low enough to minimise the collisions between the knocked out target atoms and the argon in the chamber. The effects of the ring shaped plasma can be seen in the erosion of the targets' surface. Figure 4.2 shows the clearly visible changes on the surface over time in use.

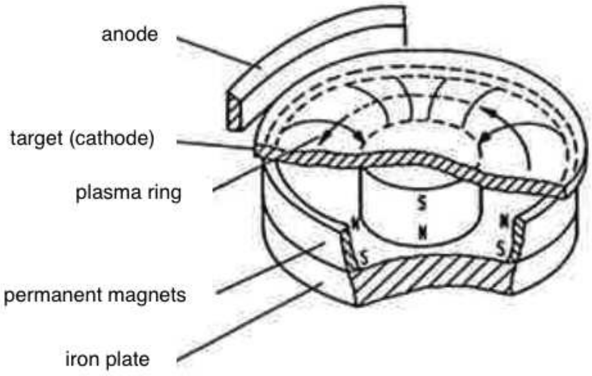

(a)

(b)

Figure 4.1.: (a) Concept of a magnetron sputter head. Courtesy of [2]. (b) Arrangement of the cylindrical permanent magnets in the sputter head, with the smaller magnets all installed in the same orientation and the larger one in the middle in the opposite direction.

(a) (b)

Figure 4.2.: (a) shows the surface of a target after only a few uses whereas (b) are the effects after long time use with a nearly 2 mm deep groove.

5. Experimental setup

The whole project started with a *Quorum SC7620* Sputter/Coater [5] with an already modified target holder for our in house produced 1 inch targets. A few early identified problems were relatively easy to solve. The built-in leak valve was worn out and starting to fail. The valve was replaced with a more robust and finer adjustable needle valve. Following this, the plumbing between vacuum chamber, valves and argon source was renewed. An external vacuum gauge was added to replace the broken internal gauge. Later it turned out, that the internal power supply, in combination with the control unit, were at their limit and could not sustain the sputtering process. Sadly, reverse engineering and modifying the large parts of the internal electronics only led to minor improvements. Therefore, the decision was made to disconnect all the internal electronics and instead power the sputter with an external adjustable high voltage power supply.

With all these changes made, there was still a problem with the sputter head to solve. Every once in a while the plasma cloud seemed to form inside the sputter head instead of in front of it. After checking for insulation errors and leaking vacuum seals, it turned out to be a design flaw of the over all sputter head geometry. A redesigned and newly made sputter head finally solved this problem.

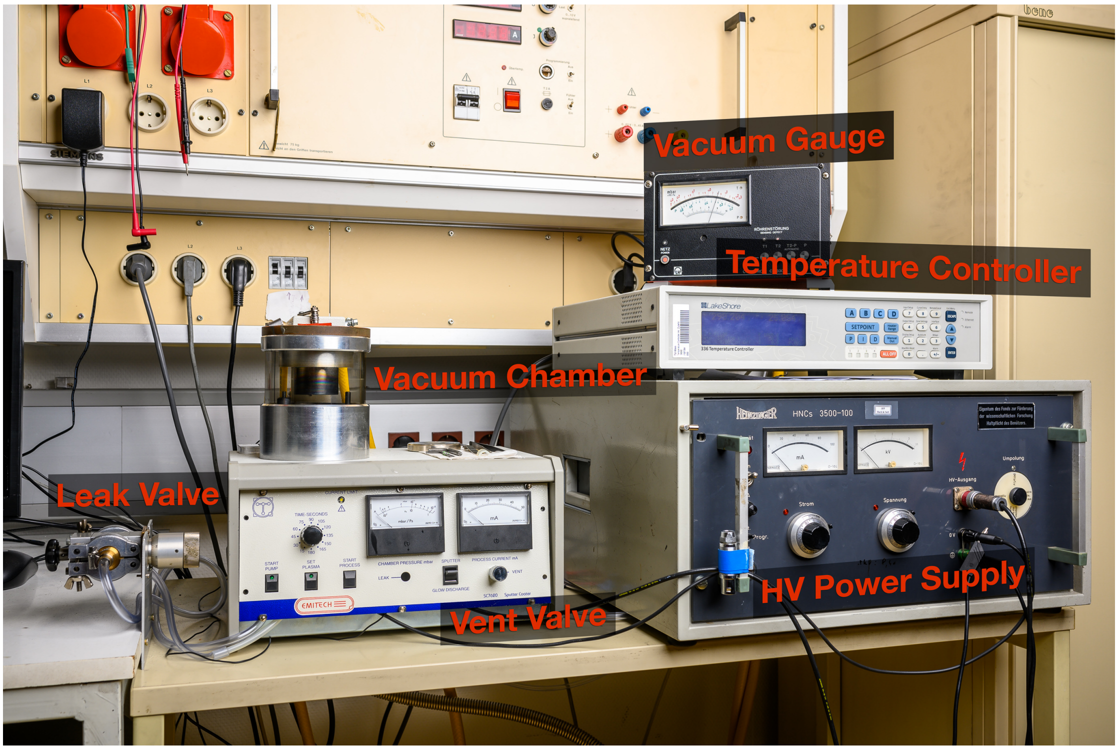

Figure 5.1.: The main components of the installation: on the left is the leak valve next to the vacuum chamber with the sputter head inside. The vent valve is mounted on the otherwise unused front panel of the chassis. On the right side, from top to bottom, are the vacuum gauge, the temperature controller for the substrate heater and the high voltage power supply.

Vacuum Pump

The vacuum pump is located on the floor below the installation and is connected to the back of the chamber via a valve, as seen in figure 5.2. The sensor for the pressure gauge and the wire feed through to the temperature controller are connected to the vacuum plumbing.

Figure 5.2.: Behind the vacuum chamber are the valve to the vacuum pump, the pressure sensor (blue) and the electrical connections for the temperature controller. The water cooling plate on top of the vacuum chamber is connected via the yellow hose.

Pressure Gauge

A Leybold *Combitron CM330* is used to monitor the pressure in the vacuum chamber. The sensor is placed next to the vacuum valve behind the chamber.

Temperature Controller

To heat up the substrate and keep it at the desired temperature the *LakeShore 336 Temperature Controller* with PID regulation is used [3]. It controls the heating elements and the temperature sensor below the substrate table.

High Voltage Power Supply

A *Heinzinger HNCs 3500-100* adjustable high voltage power supply is used as power source for the sputter head. It has a variable output voltage of 0 - 3500V and current range of 0 - 100mA. This device allows for an easy and accurate adjustment of the plasma wattage.

Leak Valve

The black knob on the left is for opening and closing the valve. The right side of the leak valve is for adjusting the argon flow rate.

Vent Valve

The vent valve is used to flush the sputter chamber with argon and to re-pressurise the system. It is installed parallel to the leak valve.

Water Cooling

On top of the chamber lid is a water cooled copper plate that is used as a heat sink for the sputter head.

Vacuum Chamber

The vacuum chamber is the heart of the whole experimental setup and contains the substrate table and the sputter head.

Substrate Table

The bottom of the chamber is occupied by the substrate table. It can be adjusted in height by a few millimetres with the screw on the left side. The hollow screw on the right holds the table in place and is connected to the argon inlet underneath the chamber. The copper block with heat elements and temperature sensors is mounted to the underside of the table.

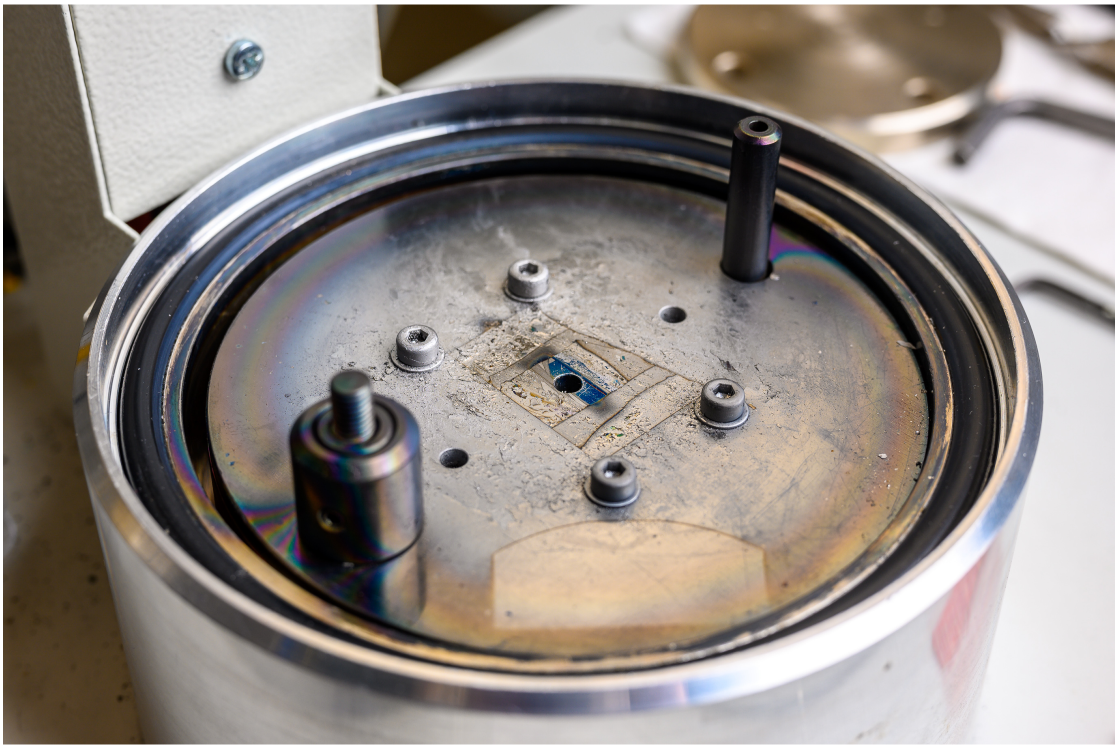

Figure 5.3.: Shown is the substrate table on the bottom of the sputter chamber. The height adjustment screw can be seen on the left side and the hollow metal pin on the right, which is the argon inlet. The four smaller screws around the centre are the mounting of the temperature controlled copper block underneath.

Sputter Head

The sputter head consists of an outer shell (anode) which is mounted to the lid with two screws. It encases the cathode excluding the area directly in front of the target, as shown in figure 5.4. With the anode removed, the whole assembly of the cathode is visible. The back of the aluminium piece is insulated to the lid and connected to the negative side of the power supply through a hole in the middle of the lid. Next is a thin Iron plate which functions as a pole shoe with a copper disc on top of it. This copper disc houses the permanent magnets. On the top of the cathode the target is held in place by an aluminium ring screwed all the way down to the aluminium cylinder. The dismantled top part of the cathode can be seen in figure 5.5.

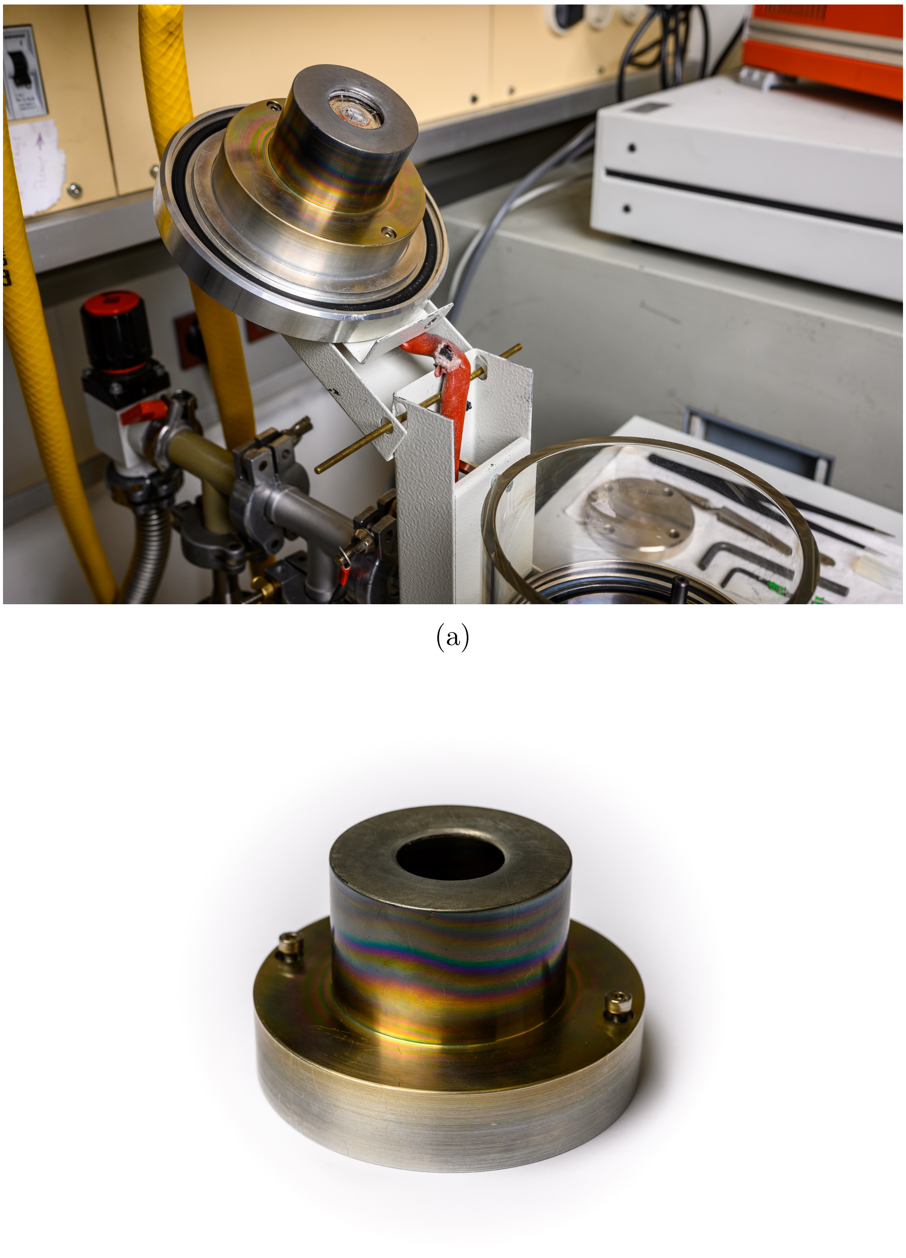

(a)

(b)

Figure 5.4.: (a) Opened lid of the vacuum chamber with the fully assembled sputter head. The installed target can be seen in the middle through the opening in the anode. (b) The outer shell of the sputter head (anode) on its own.

(a) (b)

Figure 5.5.: (a) Disassembled target holder. Aluminium ring with mounting screws and a sputter target placed on top of the copper disk. (b) Permanent magnets inside the copper disc with a thin iron plate underneath.

6. Design and Construction Process

Early tests with the *Quorum SC7620* Sputter/Coater combined with the first version of the newly designed magnetron sputter head showed that the internal power source was not powerful enough for the modified design. The lack of regulation was a drawback as well. Therefore, the internal controller and power supply of the machine were disconnected and a high voltage supply was used instead. See chapter 5 for a detailed description of the experimental setup. A 5 kΩ high power resistor remained in the circuit. This has to be accounted for when the plasma voltage or plasma wattage needs to be determined as followed:

$$U_{plasma} = U_{source} - I_{plasma} \cdot R_{5k\Omega}$$

$$P_{plasma} = U_{plasma} \cdot I_{plasma} \, .$$

A new pressure gauge was connected to the vacuum plumbing on the back and water cooling was installed. The worn out needle valve for fine regulation of the argon flow was replaced.

Geometry of the Sputter Head

With a sufficient power source in place, the next step was to find a method to consistently generate the plasma in front of the target. With the first iteration of the sputter head this was not the case. Every now and then, no visible plasma ring formed in front of the target, despite the correct power draw from the high voltage supply. Further investigation showed, the plasma cloud formed inside the sputter head next to the copper ring, right where the diameter of the assembly changed

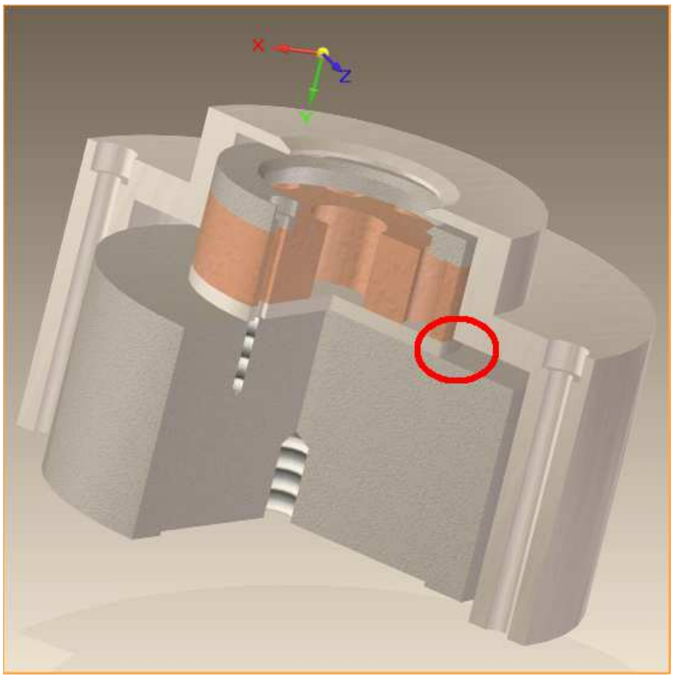

Figure 6.1.: Shown is the CAD drawing of the first iteration of the sputter head. The problematic area where the iron pole shoe meets the aluminium cylinder is marked red. The area around this corner had just the right conditions in combination of electric and magnetic field for the sputtering process to take place there instead of the desired spot in front of the target.

(figure 6.1). Redesigning the sputter head and moving the change in diameter further away from the magnets finally solved this problem (figure 6.2). Technical drawings of the modified parts can be found in appendix A.

Sputtering of Geometric Shapes

The ability to produce these shapes is shown in figure 6.3, where a test sample of alternating materials in a snake-like pattern was produced in two steps with a simple paper screen on top of the substrate. This method allows for the production complex constructs like multi-stage thermoelectric generators. With more robust screens even finer shapes would be possible.

Figure 6.2.: Redesigned sputter head with the change to a wider diameter, closer to the chamber lid. Making the aluminium cylinder the same diameter as the rest of the cathode led to a uniform electrical field and removed the perpendicular space next to the pole shoe. The step to a wider diameter near the lid is still necessary for the vacuum seal to fit, but it is no longer a problem at this distance from the magnets.

Figure 6.3.: Test sample of a multi-stage thermoelectric generator with alternating materials. The shape was produced in two steps with a screen (shown on the right) for each material used. The dimensions of this pattern are 20 mm by 25 mm.

7. Sputter Operating Manual

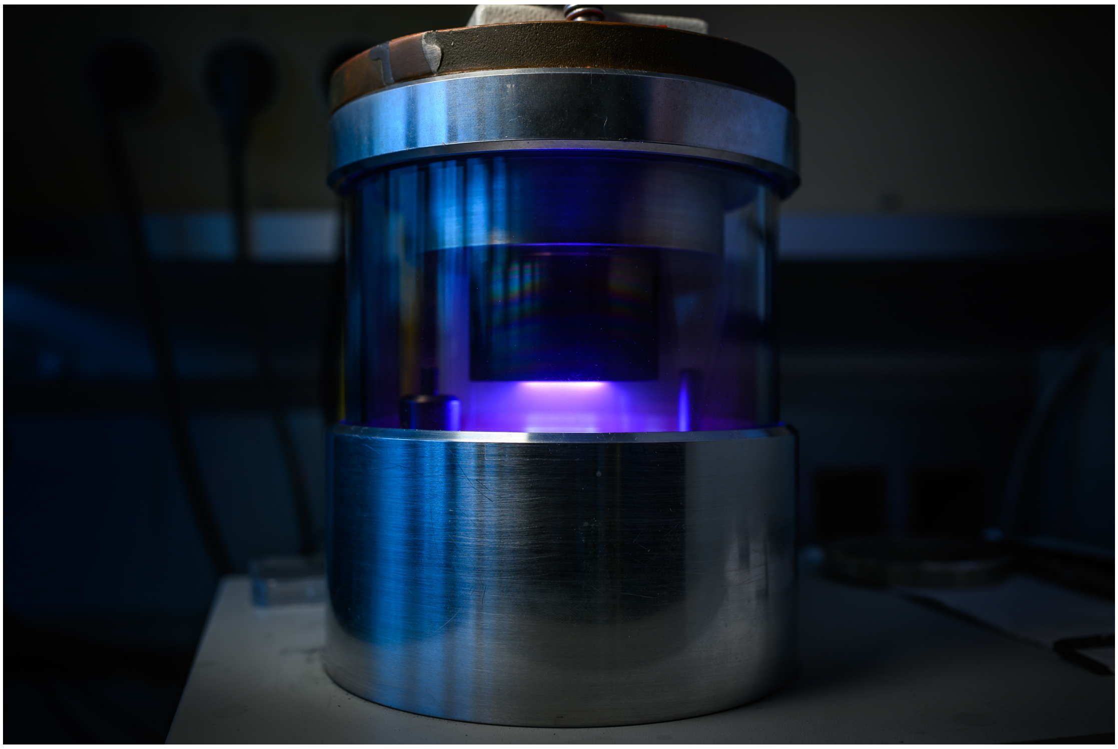

This chapter is a manual on how to use the sputter. It is aimed at avoiding operating errors and finding a suitable starting point. However the given numbers are guidance values only. The actual values differ from target to target.

7.1. Preparation

The first steps are to turn on the cooling water, open the argon source and close the valve to the vacuum pump. Then the pump should be turned on and the

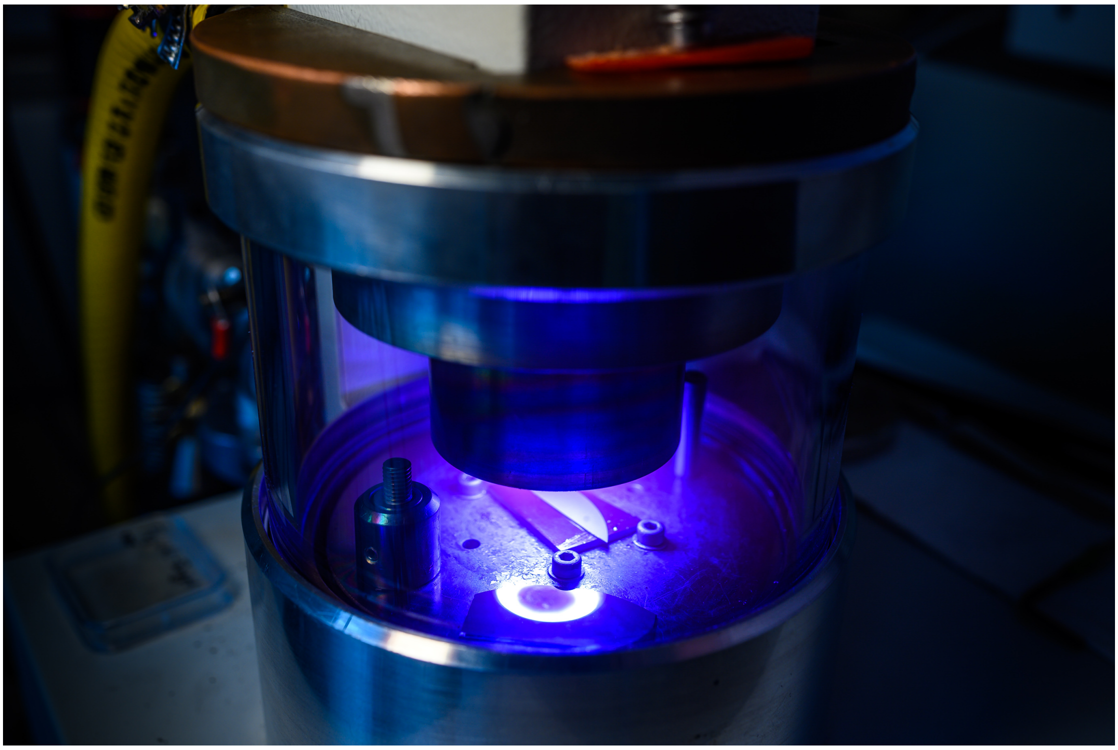

Figure 7.1.: This picture shows the sputter during operation. The dark violet colour of the emitted light indicates an stable plasma and ongoing sputtering. The plasma ring can be seen via a mirror placed on the front area substrate table. Directly underneath the sputter head is a piece of glass with a semicircular piece of silicone wafer on top of it. This placement allows for the thickness to be measured an the straight edge on the glass. The coated wafer can be used for further treatment and measurements.

temperature controller set to the desired substrate temperature. The vent valve and the leak valve should be closed. Place a clean substrate ready to coat in the middle of the chamber and close it. Putting a glass sheet underneath the substrate allows for an easier measurement of the film thickness. Carefully open the valve to the vacuum pump. Make sure the substrate stays in place. After two to three minutes open the vent valve for two seconds to flush the chamber with argon. If the argon bottle was closed before, then wait for a few more seconds to flush the whole argon tubing. Wait for at least 10 minutes to get a clean vacuum. Flush the chamber again for two seconds and wait for another two to five minutes. If necessary, wait until the substrate holder reaches its set temperature.

7.2. Getting the Plasma Started

Open the leak valve and adjust it to a chamber pressure between 4 and 10 µbar. Turn on the high voltage power supply and set it to about 800 V. If the current is still zero, slightly flush the chamber with the vent valve. As soon as the plasma starts, close the vent valve. The plasma current should be somewhere around 70 to 100 mA. The pressure falls back to the before set value. The colour of the plasma may be white/light orange at the beginning. When the pressure is low enough, the plasma should clearly visibly change to a dark violet colour. This is the indicator that the sputtering process is starting and the target material is transported to the substrate. Now, start the timer for the desired sputtering duration and adjust the voltage until you reach your desired plasma current of about 40 mA. If the current is set too low, the sputtering may stop again, indicated by the plasma colour changing back to white or orange. In this case, you need to go back to a higher current until the colour changes back. Then, set the plasma current again. If the chamber pressure gets too low (<2 µbar), the plasma may stops completely. In that case you need to flush the chamber again. It could be necessary to readjust the chamber pressure a little bit within the first tree minutes. After changing the pressure, always check the plasma current and readjust if necessary. Let the calculated time, depending on the expected sputter rate and the desired thickness of the film, pass.

7.3. Finishing

After the sputtering is finished, turn the voltage to zero to stop the process. Close the valves to the vacuum pump and the leak valve. Now open the vent valve to fill the chamber with argon until you are able to open the lid. For safety reasons, put the ground probe in contact with the target to discharge any capacities! Now you can measure the target temperature if needed. Put the coated substrate on a heat sink to cool down and place a new substrate in the chamber to start again.

7.4. Servicing

After about twenty sputter cycles, the permanent magnets behind the target need to be checked. Because of the high temperatures the sputter head can reach during operation, the magnetisation can be weakened. Checking the magnets can be done manually by holding them against a piece of iron one by one. Weakened magnets need to be replaced. A second method of identifying broken magnets is via a small deformation of the plasma ring, but this is hard to spot. From time to time, some of the sputtered material on the head around the target can splinter and short the circuit between anode and cathode or drop down on the substrate. In this case the aluminium ring holding the target in place and the rim of the anode need to be cleaned with acetone in order to get rid of the loose pieces. During operation, the inside of the glass cylinder is slowly coated with target material and gets more opaque over time. To clean the cylinder, submerge it in slightly diluted nitric acid (HNO_3) for a few minutes to get rid of the staining.

8. Measurements

To verify the produced Heusler thin films, various measurements were made. At first the film thicknesses of the films were assessed with the help of a profilometer. During the build phase of the experimental setup this was necessary to check if the sputter process was working correctly and enough material was transported to the substrate. The thickness was an important indicator to find out which variables had the highest influence on the functionality. For example, early tests showed that nine outer magnets plus one in the middle and a lower argon pressure was more reliable than a six plus one magnet configuration at a higher argon pressure. The used parameters for each produced sample can be seen in tables A.1 and A.2. Later in the sputter build process, when the produced thin films were consistent, further measurements were made. X-Ray diffractograms showed the crystal structure of the films and were able to verify, that they match the structure of the used target materials. The electrical resistance and the Seebeck coefficient were measured in dependence of the temperature, which yielded results comparable to known similar samples.

8.1. Film Thickness

The film thickness was measured with the help of a profilometer as seen in figure 8.1a. Each film was measured on at least five different points to get a mean thickness and a sense of the variance of the thickness across each sample (figure 8.1b). To allow for the step height measurements, the films were always sputtered on two substrates at once, a glass sheet underneath and a smaller piece of silicon wafer on top of it (figure 8.2). The sputtered wafers were used for further treatments and measurements, whereas the glass substrates were mainly used for the determination of the film thickness. For consistency, only the unpolished side of the wafers was used to keep the influence of varying substrate surfaces at a minimum. An example of an evaluated measurement can be seen in figure 8.3. The curve represents the height along a 1,25 mm long line across the step from the coated to the uncoated surface.

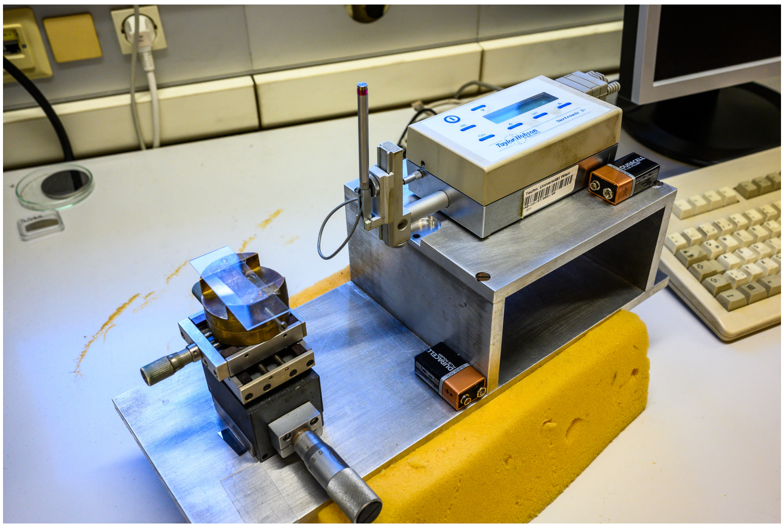

(a)

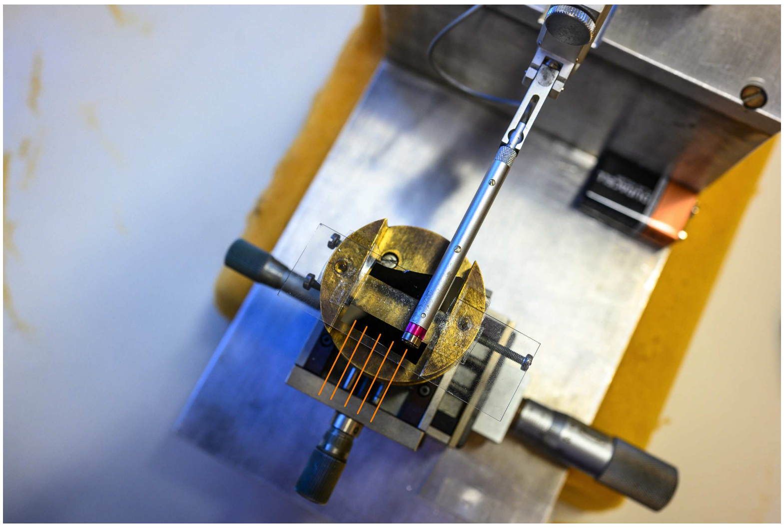

(b)

Figure 8.1.: (a) Computer aided Taylor Hobson profilometer used for surface profile measurements. (b) Visualisation of the five equidistant measurement points for each sample with the sensor arm in place for the first one.

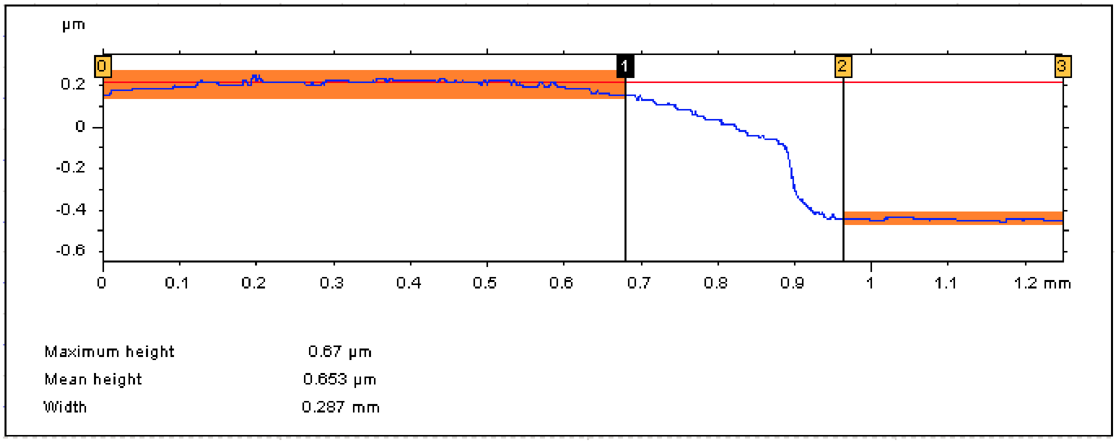

Figure 8.3.: Example of a step height measurement analysed and plotted with the software TalyProfile. The measurement runs from the coated surface across the edge to the uncoated glass surface. After defining the high and low areas of the plot, the software calculates the mean height difference. This example is one of the five measurements of sample 02WB08 with a mean height of 0,653 µm.

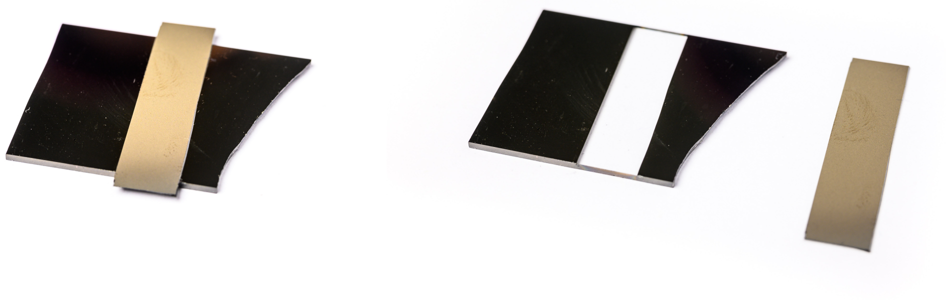

(a) (b)

Figure 8.2.: (a) Silicon wafer on top of the glass sheet. This is the arrangement they were placed in the sputter and coated from above. (b) Sputtered glass and silicon wafer next to each other with the step from glass surface to film for film thickness measurements.

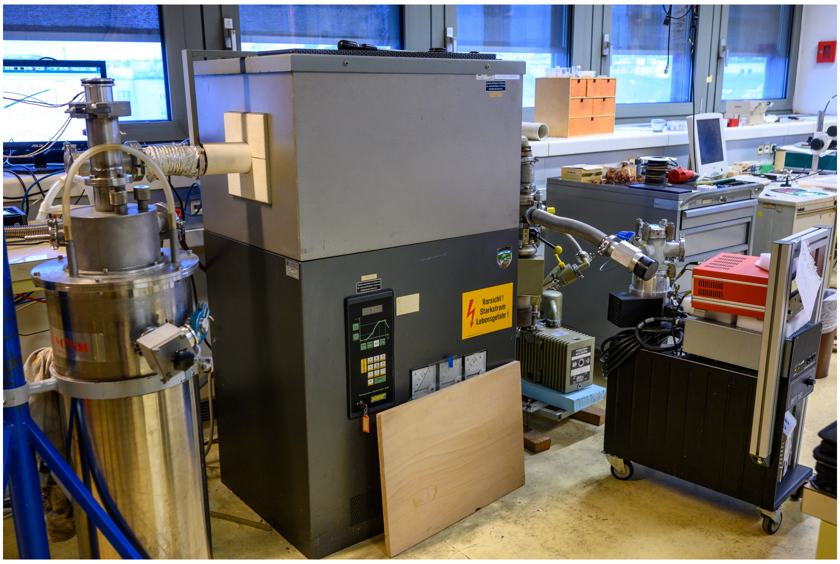

Figure 8.4.: Vacuum oven used for the heat treatment of the thin films to reduce tensions and defects in the lattice.

8.2. Heat Treatment

The Heusler thin films were then put into a vacuum oven. This heat treatment lead to a reduction of tensions and defects in the lattice which can occur during the growth of the thin film in the sputter and causes the initially almost amorphic state to crystallise. As seen in the thesis of Alexander Riss [9] the most effective treatment of these films is at 450 °C over the time of seven days. Therefore, these parameters were used for all the samples. Figure 8.4 shows the vacuum oven with its connected vacuum pump. Thanks to the relatively large volume of the heating chamber it was possible to treat multiple samples at once.

8.3. XRD Analysis

For verification of the films' crystal structure, a *PANalytical XPert Pro MPD* $\theta - \theta$ x-ray diffractometer (figure 8.5) was used. The diffractometer uses a $\theta - \theta$ configuration with a Cu K_α x-ray source, sample and detector to measure the

Figure 8.5.: *XRD device PANalytical XPert Pro MPD* at the X-Ray Center Getreidemarkt, TU Wien.

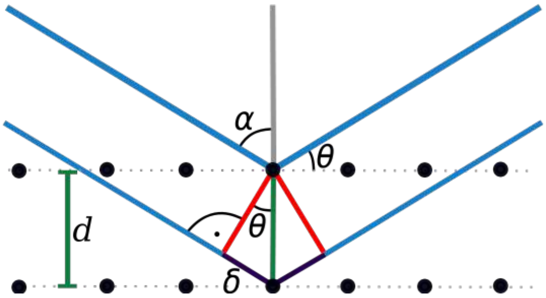

Figure 8.6.: Geometric explanation of the Bragg equation [1].

reflected x-ray beam. The Bragg equation

$$2d\sin\theta = n\lambda$$

says the reflection of the x-ray beam from different lattice planes interferes with itself constructively when the difference of the path length is a multiple of the wavelength of the beam (figure 8.6). Therefore, peaks at angles θ represent lattice plane distances d in the sample. The XRD diffractograms in figure 8.7 show, if the typical Heusler peaks are present, which indicates that the film formed the desired crystalline structure of the target material. Different peaks represent the different planes within the specific Heusler lattice. Besides large peaks at 33°and 70°caused by the silicon wafer used as substrate [10], the reflexes caused by the Heusler lattice are visible at 44°, 64° and 82°, which correspond with the planes (110), (200) and (211) of the here used Heusler compound $Fe_2V_{0.8}W_{0.2}Al$. An explanation for the very small peak at 82° could be a preferred orientation of the structure in the thin film. The expected diffractogram of Fe_2VAl Heusler compound with the lattice parameter a = 5,76 Å is plotted for comparison. The XRD measurements are leading to the assumption, that the thin films are of a cubic structure as the target material, but the absence of the (111) and (200) peaks at low angles indicates a transformation of the classical Heusler structure (Cu_2MnAl-type) to the cubic W-type, where all individual elements of the material are distributed statistically on all lattice sites. More details about this phenomenon can be found in [8]. For further confirmation of the sample quality, the Seebeck coefficient of some samples was also measured.

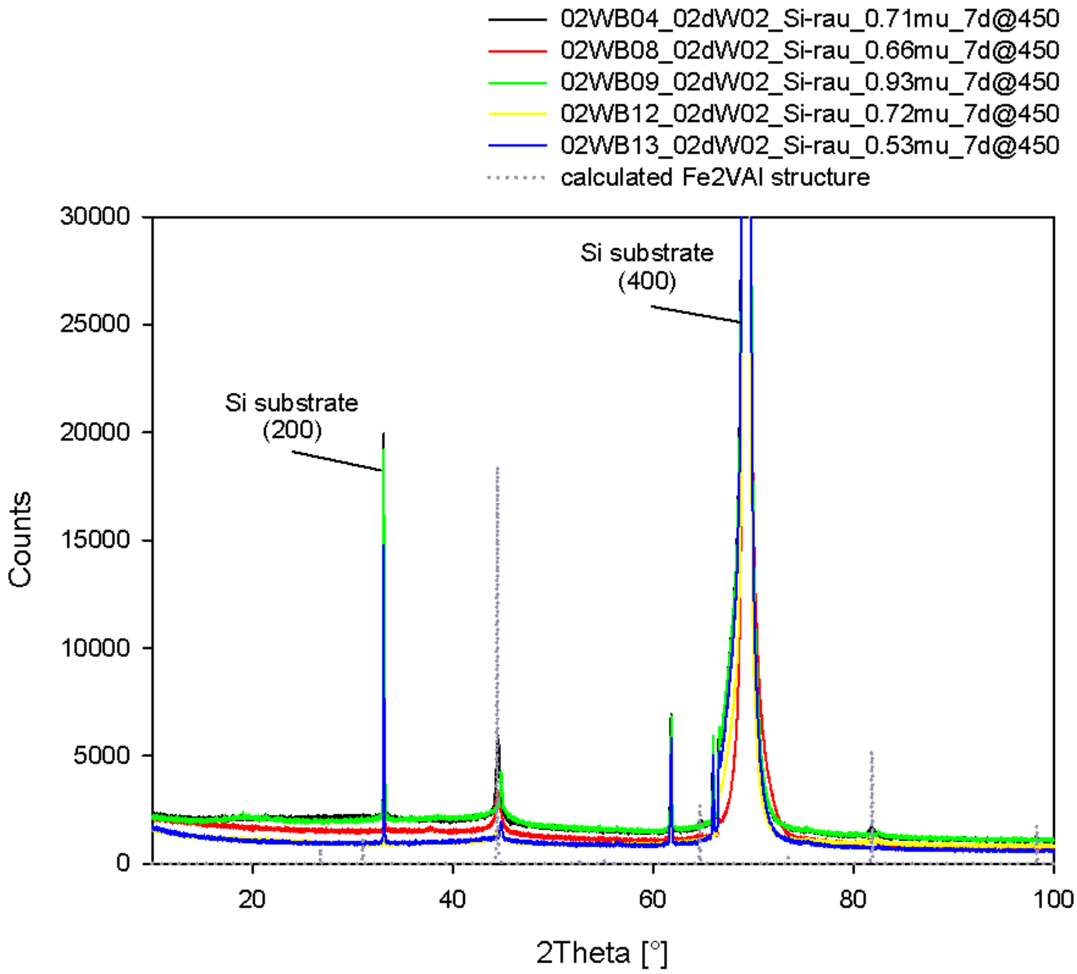

Figure 8.7.: Combined x-ray diffractogram. Reflections caused by the Heusler lattice are visible at 44°, 64° and 82°, which correspond to the planes (110), (200) and (211) of the Heusler compound $Fe_2V_{0.8}W_{0.2}Al$. The dotted line is the expected diffractogram of Fe_2VAl with the lattice parameter a = 5,76 Å and space group 225.

8.4. Thermoelectric Properties

The thermoelectric properties of the coated wafers were measured with the help of a *ULVAC ZEM3* for automatic Seebeck and electric resistivity measurements (figure 8.8). The substrate was mounted on a sample holder for thin films (figure 8.9). The sample was mechanically secured between the larger contacts on both ends.

Two additional probes were brought in contact with the surface of the film. The chamber was then closed and evacuated. After flushing with Helium three times, the measurement was started. The temperature was then ramped up from room temperature to 475°C and down again with measuring points at fixed temperatures. At each of these measurements, a temperature difference between the top and the bottom of the sample was applied. The exact temperature difference as well as the difference of the electrical potential were measured. This lead to the Seebeck coefficient

$$S(T) = \frac{U(T)}{\delta T} \,,$$

with $U(T)$ being the measured voltage the average temperature T between the two probes and δT the temperature difference. Additionally, the electrical resistivity was measured at every one of these steps. Therefore, a known current was sent through the outer contacts while the inner two measure the potential difference. With

$$R(T) = \frac{U(T)}{I}$$

and the known geometry of the sample, the specific resistivity $\rho(T)$ can be calculated. With $S(T)$ and $\rho(T)$ the power factor PF can be plotted. In the figures 8.10 and 8.11 these three plots are shown for sample 02WB08. In comparison, similar $Fe_2V_{0.8}W_{0.2}Al$ thin films produced in another sputter showed maximum PFs between 20 and 40 $mW/m{\cdot}K^2$. $Fe_{1.6}Cr_{0.4}VAl$ films had a PF of up to 200 $mW/m{\cdot}K^2$. A calculation of the band structure with help of the Seebeck measurement was tested and can be seen in figure A.3 in the appendix. The results showed, that the thin film samples produced with the built sputter are of sufficient quality and the machine can be used for further production of various Heusler thin film samples. With this sputter it is possible to produce higher quantities of different Heusler films and speed up future research.

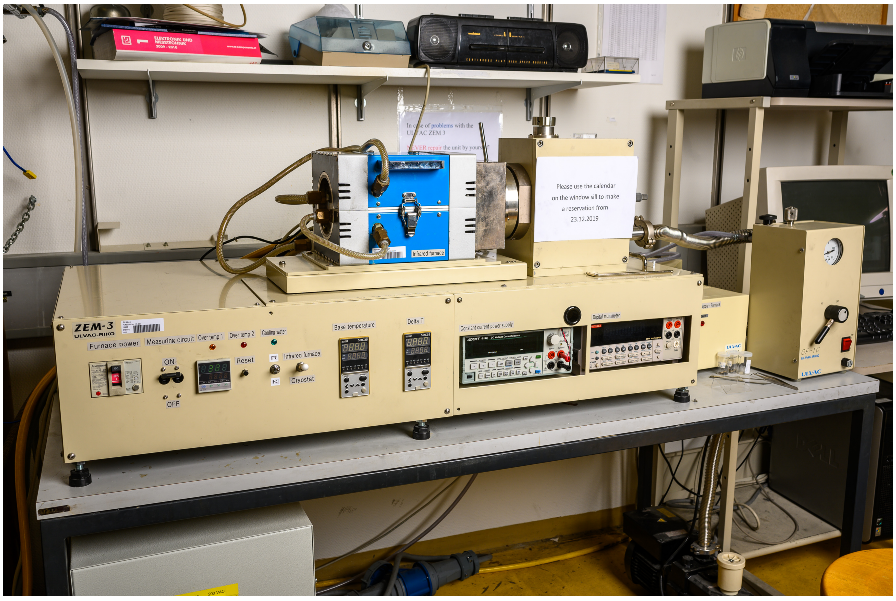

Figure 8.8.: *ULVAC ZEM3* for Seebeck and electric resistivity measurements.

Figure 8.9.: Sample holder used to measure thin films with the *ULVAC ZEM3*.

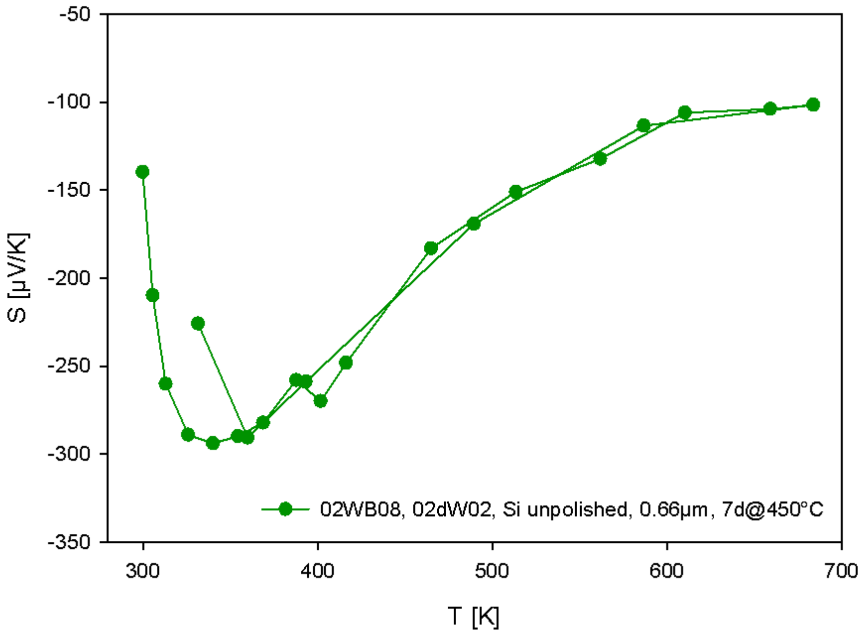

(a)

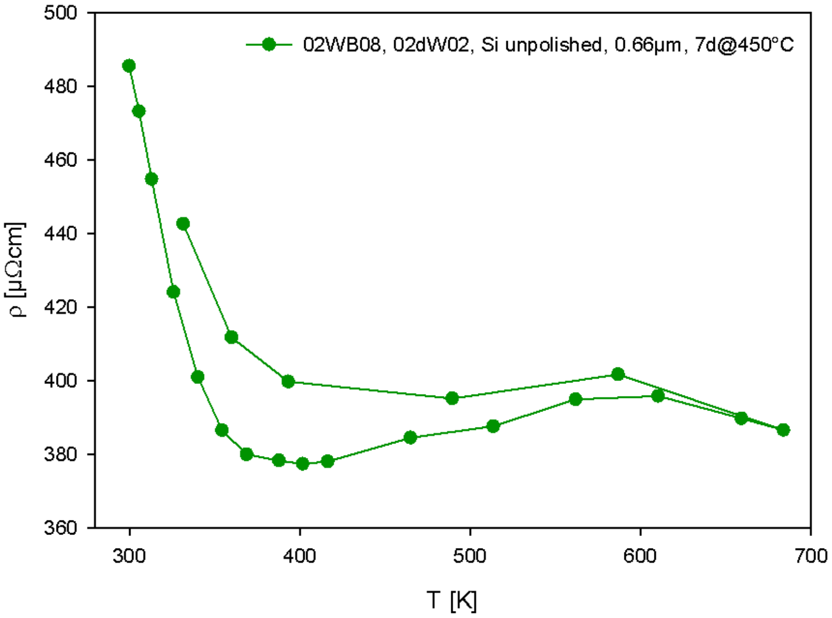

(b)

Figure 8.10.: Seebeck coefficient (a) and the specific resistivity (b) of the sample 02WB08 with a thickness of 0.66μm after the thermal treatment of 7 days at 450°C. Measured with *ULVAC ZEM3*.

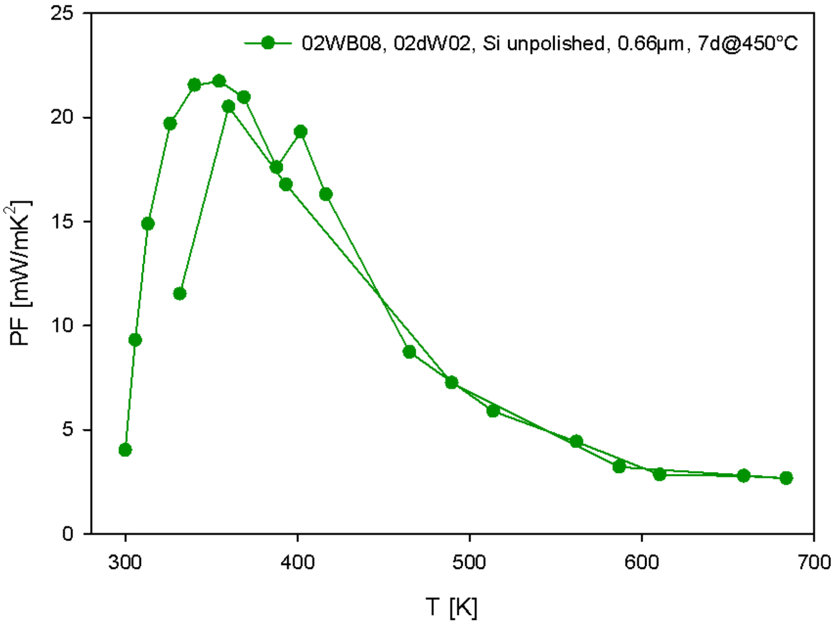

Figure 8.11.: Power factor of the sample 02WB08.

9. Conclusio

In the context of this diploma thesis a new DC magnetron sputter installation was designed, built and put in operation. It started with the modification of an existing sputter/coater to be able to produce Heusler thin films, which have very promising thermoelectric properties. The switch from the internal controller and power supply of the initial machine to an external setup with a dedicated adjustable high voltage power supply was one of the first important decisions. The ability to control the current in addition to a more powerful source was mandatory to build the sputter in the desired configuration. The upgraded leak valve in combination with a precise vacuum gauge made it possible adjust and stabilise the plasma and therefore the sputter rate. At a plasma power of about 13 watts, a stable sputter rate of 0,07 µm can be achieved.

Measurements of the Seebeck coefficient and the XRD analysis have shown, that the produced thin films have a sufficient quality. Therefore, the new sputter is suitable for further research on thermoelectric properties of Heusler materials. The faster production of thin film samples makes it easier to test the influences of small variances of the large amount of possible parameters in higher quantities. With the possibility of sputtering different geometric shapes with the help of templates, the analysis of more complex shapes like multi-stage thermoelectric generators is a possibility.

Possible future enhancements

During the work with the finished sputter near the end of this diploma thesis, a few possible improvements came to light. A more direct cooling solution of the target holder would help to keep the target temperature at a lower level during longer sputter periods. This would potentially increase the lifetime of the $Nd_2Fe_{14}B$ permanent magnets in the sputter head. The first minute of the sputtering process can be a bit unpredictable until the plasma stabilised. The addition of an externally controlled shutter mechanism between sputter head and substrate would allow to exclude the uncertain starting process of the sputter and therefore provide an even finer control of the produced film thicknesses.

A. Appendix

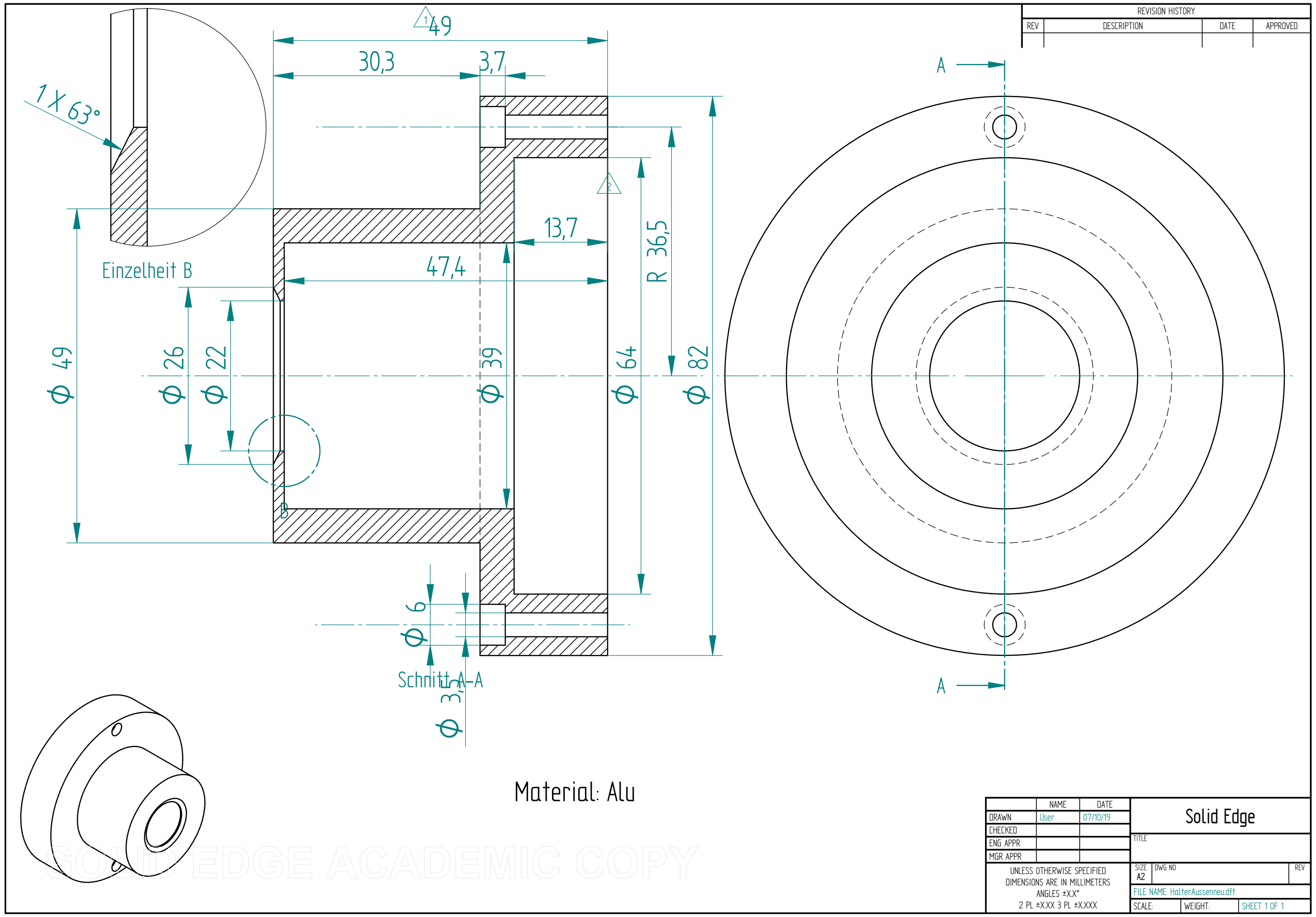

Figure A.1.: CAD drawing of the modified outer shell of the sputter head.

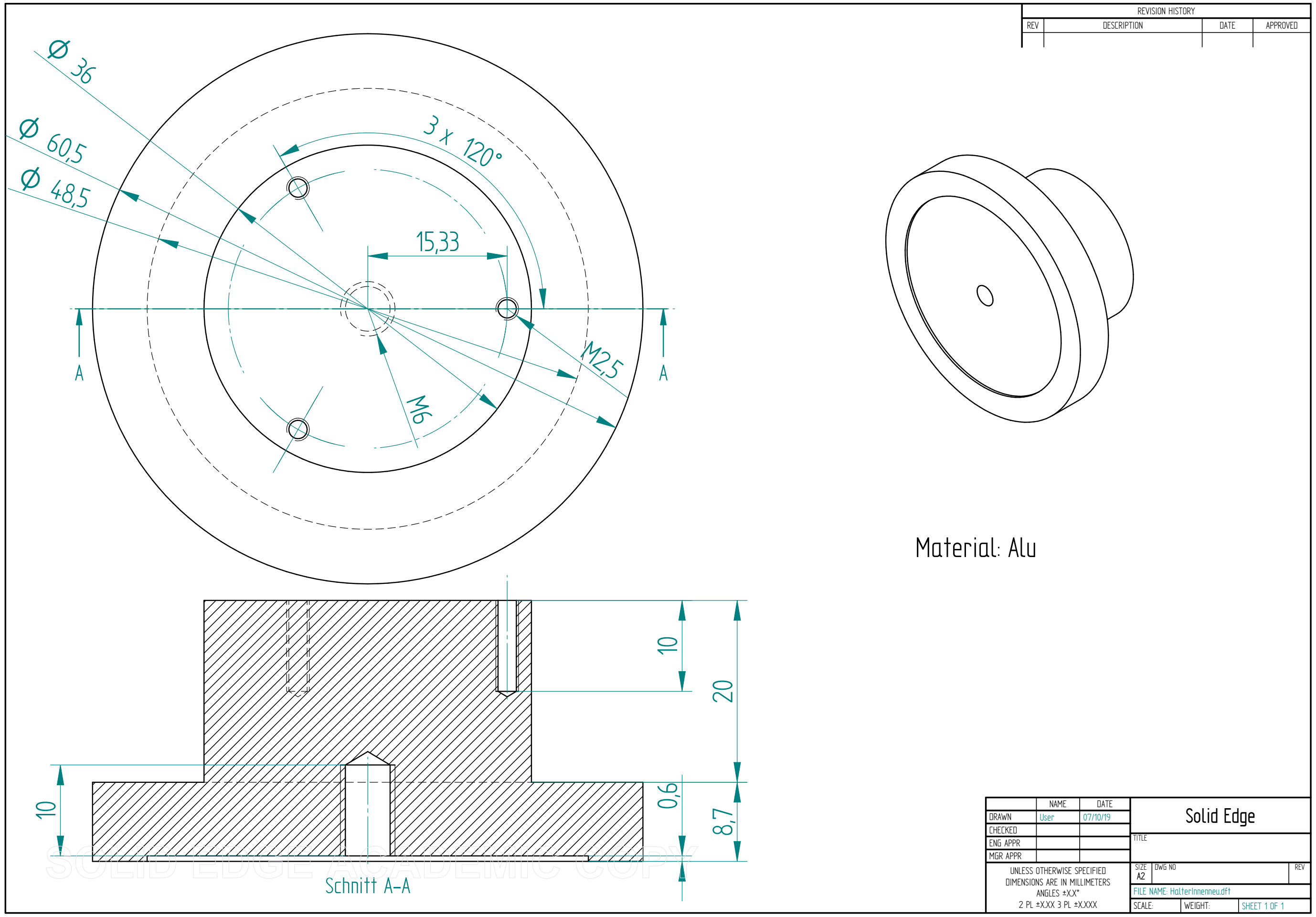

Figure A.2.: CAD drawing of the modified back part of the cathode.

sample name	target	sub temp [°C]	U_plasma [V]	I [mA]	P_plasma[W]	p [µbar]	time [min]	T_target [°C]	thickness_avg [µm]	sputter rate [µm/min]
02Co B6	Co 0,2	30	300	100	30	40	10	72	1,15	0,115
02Co B7	Co 0,2	30	300	100	30	40	10	160	0,59	0,059
02Co B8	Co 0,2	25	300	100	30	40	15	145	0,87	0,058
02Co B9	Co 0,2	30	300	100	30	20	15	115	1,37	0,091
02Co B10	Co 0,2	35	300	100	30	80	11	130	0,63	0,057
02Co B11	Co 0,2	30	300	100	30	20	15	135	1,44	0,096
02Co B12	Co 0,2	25	320	100	32	20	10	145	0,92	0,092
02Co B13	Co 0,2	30	320	100	32	20	20	175	1,84	0,092
02Co B14	Co 0,2	35	320	100	32	20	30	140	n/a	n/a
02Co B15	Co 0,2	30	320	100	32	20	10	125	0,96	0,096
02Co B16	Co 0,2	30	330	50	16,5	20	10	95	0,72	0,072
02Co B17	Co 0,2	30	300	30	9	20	10	75	n/a	n/a
02Co B18	Co 0,2	30	290	30	8,7	20	10	70	0,49	0,049
02Co B19	Co 0,2	35	350	100	35	10	10	190	1,09	0,109
02Co B20	Co 0,2	30	290	100	29	20	10	140	1,33	0,133
02Co B21	Co 0,2	35	290	100	29	20	10	170	0,80	0,080
02Co B22	Co 0,2	25	290	100	29	20	10	140	0,67	0,067
02Co B23	Co 0,2	25	250	50	12,5	20	10	75	n/a	n/a
02Co B24	Co 0,2	30	300	100	30	20	10	105	1,05	0,105
02Co B25	Co 0,2	30	280	70	19,6	20	10	85	0,43	0,043
02Co B26	Co 0,2	30	300	50	15	20	10	65	0,29	0,029
02Co B27	Co 0,2	30	290	40	11,6	20	10	55	0,26	0,026
02Co B28	Co 0,2	25	270	70	18,9	20	10	75	0,43	0,043
02Co B29	Co 0,2	30	260	30	7,8	20	10	45	n/a	n/a
02Co B30	Co 0,2	30	260	30	7,8	20	10	40	n/a	n/a
02Co B31	Co 0,2	30	290	50	14,5	20	10	60	0,40	0,040
02Co B32	Co 0,2	25	290	50	14,5	20	20	65	0,71	0,036
02Co B33	Co 0,2	25	280	50	14	20	30	60	1,07	0,036

Table A.1.: Sputtering parameters of different samples used in the performed experiments, part 1 of 2.

sample name	target	sub temp [°C]	U_plasma [V]	I [mA]	P_plasma[W]	p [µbar]	time [min]	T_target [°C]	thickness_avg [µm]	sputter rate [µm/min]
02Co B34	Co 0,2	25	280	50	14	20	40	70	1,40	0,035
02Co B35	Co 0,2	80	270	50	13,5	20	20	70	0,71	0,036
02Co B36	Co 0,2	110	270	50	13,5	20	20	65	0,67	0,034
Fe2V B01	Fe2VAl	25	290	50	14,5	20	20	70	0,73	0,037
Fe2V B02	Fe2VAl	25	270	50	13,5	20	20	-	0,79	0,040
Fe2V B03	Fe2VAl	25	280	40	11,2	20	20	60	0,64	0,032
Fe2V B04	Fe2VAl	30	370	100	37	200	10	120	n/a	n/a
Fe2V B05	Fe2VAl	25	260	50	13	20	20	55	0,60	0,030
Fe2V B06	Fe2VAl	25	260	50	13	20	20	55	0,51	0,025
Fe2V B07	Fe2VAl	25	270	50	13,5	10	20	-	0,79	0,039
Fe2V B08	Fe2VAl	25	260	30	7,8	10	20	-	0,35	0,017
Fe2V B09	Fe2VAl	170	310	100	31	10	12	85	0,89	0,074
Fe2V B10	Fe2VAl	230	310	50	15,5	6	12	55	0,53	0,044
Fe2V B11	Fe2VAl	230	320	50	16	4	20	50	0,88	0,044
Fe2V B12	Fe2VAl	220	310	30	9,3	1	20	50	0,52	0,026
Fe2V B13	Fe2VAl	160	270	20	5,4	4	22	-	0,00	0,000
02W B01	02dW	30	400	70	28	10	30	-	3,79	0,126
02W B02	02dW	190	370	50	18,5	20	15	160	n/a	n/a
02W B03	02dW	130	340	50	17	7	20	140	1,50	0,075
02W B04	02dW	135	330	40	13,2	6	10	120	0,71	0,071
02W B05	02dW	45	350	50	17,5	8	10	140	0,87	0,087
02W B06	02dW	170	340	50	17	8	10	140	0,88	0,088
02W B07	02dW	150	290	30	8,7	8	10	90	0,46	0,046
02W B08	02dW	155	300	30	9	8	15	110	0,66	0,044
02W B09	02dW	165	350	50	17,5	6	10	140	0,93	0,093
02W B10	02dW	165	320	40	12,8	4	10	120	0,72	0,072
02W B11	02dW	160	330	30	9,9	2	10	95	0,65	0,065
02W B12	02dW	165	320	40	12,8	4	10	130	0,72	0,072
02W B13	02dW	175	300	30	9	6	12	90	0,53	0,044

Table A.2.: Sputtering parameters of different samples used in the performed experiments, part 2 of 2.

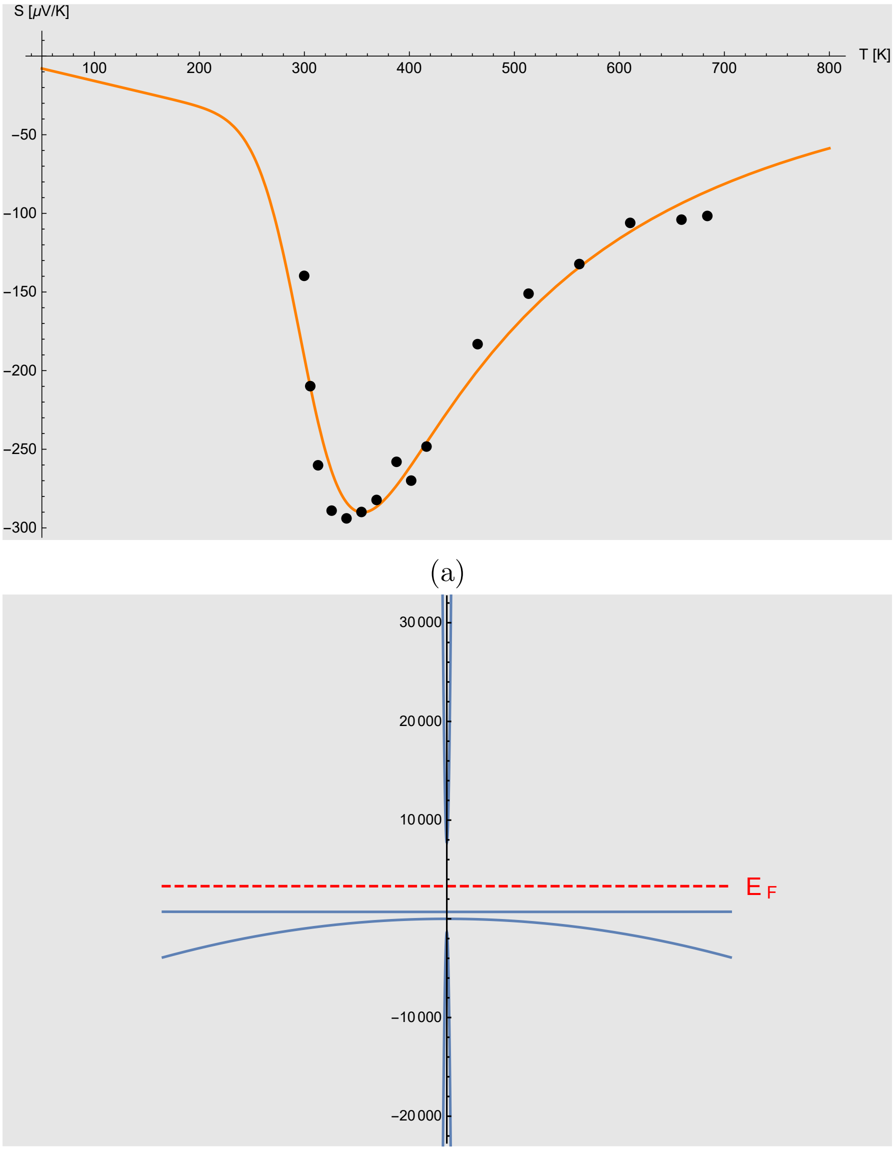

(a)

(b)

Figure A.3.: Calculation of the band structure of sample 02WB06. As depicted, a minimum of 4 bands (fit parameters) was needed to find a sufficient fit (a). The fit parameters which represent the 4 bands are plotted in (b). The Fermi energy is at 1932 K ($\frac{\epsilon}{k_B}$) and the values of the parameters are (1, 0, -1), (1, -1959, -0.000026), (1, 5509, 0.000030) and (1, 137.9, 9.50), which can be read as (degeneracy, energy offset, effective mass).

Bibliography

[1] Matthias M. (SVG-version) Dipl.-Phys. (JPG-version). *Schema zur Beugungsgeometrie.* URL: `https://upload.wikimedia.org/wikipedia/commons/c/ca/Bragg.svg`.

[2] A. Bergauer / C. Eisenmenger-Sittner. *Technologie Dünner Schichten.* 2006.

[3] Lake Shore Cryotronics Inc. “Model 336 Temperature Controller User’s Manual”. 2009.

[4] C. Kittel. *Introduction to Solid State Physics.* 7th ed. John Wiley and Sons, 1996. ISBN: 978-0471111818.

[5] Quorum Technologies Ltd. *SC7620 Mini Sputter Coater Operating Manual.* 2011.

[6] Neil W. Ashcroft / N. David Mermin. *Festkörperphysik.* 2nd ed. Oldenbourg, 2005. ISBN: 3-486-57720-4.

[7] M. Reissner / S. Bühler-Paschen / H. Michor. *Festkörperphysik I.* 2016.

[8] Tanja Graf / Claudia Felser / Stuart S.P. Parkin. “Simple rules for the understanding of Heusler compounds”. In: *Progress in Solid State Chemistry* (2011).

[9] Alexander Riss. “Herstellung und Untersuchung von dünnen Schichten, basierend auf der Heusler-Verbindung Fe2VAl, im Hinblick auf thermoelektrische Anwendungen”. master thesis. TU Wien, 2019.

[10] Peter Zaumseil. “High-resolution characterization of the forbidden Si 200 and Si 222 reflections”. In: *Applied Crystallography* (2015).